Chiral hinge magnons in second-order topological magnon insulators

Alexander Mook ⓞ, Sebastián A. Díaz ⓞ, Jelena Klinovaja ⓞ, and Daniel Loss ⓞ

Department of Physics, University of Basel, Klingelbergstrasse 82, CH-4056 Basel, Switzerland

When interacting spins in condensed matter order ferromagnetically, their ground-state wave function is topologically trivial. Nonetheless, in two dimensions, ferromagnets can support spin excitations with nontrivial topology, an exotic state known as topological magnon insulator (TMI). Here, we theoretically unveil and numerically confirm a ferromagnetic state in three dimensions dubbed second-order TMI, whose hallmarks are excitations at its hinges, where facets intersect. Since ferromagnetism naturally comes with broken time-reversal symmetry, the hinge magnons are chiral, rendering backscattering impossible. Hence, they trace out three-dimensional paths about the sample unimpeded by defects and are topologically protected by the spectral gap. They are remarkably robust against disorder and highly tunable by atomic-level engineering of the sample termination. We predict that a van der Waals heterostructure built from chromium trihalide and transition metal dichalcogenide monolayers exhibits second-order magnon topology. Our findings empower magnonics, the harnessing of spin waves as information carriers, with the tools of higher-order topology, a promising route to combine low-energy information transfer free of Joule heating with three-dimensional vertical integration.

I. INTRODUCTION

The quantum Hall effect and the Chern-insulating state of electrons are two of the great discoveries in the second half of the 20th century that have shaped today's solid state research by amalgamating Bloch's band theory with quantum state geometry and topology [1–3]. One of the many novel exotic phases of matter brought to light by this fruitful synthesis is that of the topological magnon insulator (TMI), a two-dimensional phase that exhibits a spectrum of topologically nontrivial bosonic excitations, called magnons, above a topologically trivial magnetically ordered ground state [4–9]. A topologically nontrivial gap in the magnon spectrum protects magnonic edge states. Due to time-reversal violation in ferromagnets, the propagation of the edge modes is chiral akin to electronic Chern insulators, giving rise to magnon Hall effects [10–17]. Hence, TMIs support unidirectional magnon currents that, once coherently excited, transfer information along the sample's boundary [4,5]. In sharp contrast to electrons, the charge-neutral magnonic currents do not cause Ohmic heating [18], promising low-energy information transfer and giving rise to the paradigm of "topological magnonics" [19–22]. However, since the magnonic Chern insulator is a two-dimensional phase of matter, it is not suitable to keep up with information technology design trends such as three-dimensional vertical integration [23].

Herein, we contribute to the foundations of topological magnonics by reporting our theoretical discovery of an exotic phase of matter in three dimensions dubbed second-order TMI (SOTMI). In general, the hallmarks of a higher-order (or *n*th-order) topological phase in *d* dimensions are gapless states at its *n*th-order boundaries ($n \geqslant 2$) [24–26]. So far, second-order ($n = 2$) topological magnons have been identified as *localized* corner states in two-dimensional magnets [27–29]. In contrast, we present a SOTMI in three dimensions,

whose hinges, the intersections of facets, support *propagating* gapless chiral magnons, as depicted in Fig. 1. These hinge magnons trace out a three-dimensional path, allowing
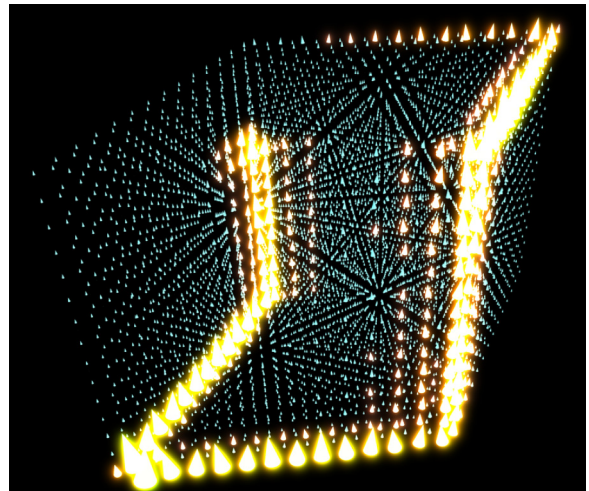

FIG. 1. Snapshot of a chiral hinge magnon in a SOTMI visualized by atomistic spin dynamics simulations. At each lattice site of a stack of honeycomb layers, a classical spin vector is represented by a little cone, whose size encodes its deviation from the ferromagnetic ground state. Large cones indicate strongly excited spins. Since the magnon spectrum exhibits a gap, within which topologically protected states only exist at the hinges of the sample, a coherent local excitation at one of the hinges (here: in the middle of the rearward left hinge) launches a unidirectionally propagating spin wave. The snapshot is taken before the spin wave completed the loop along the hinges. The topological protection due to the absence of backscattering renders the chiral hinge magnon remarkably robust against defects and disorder.

for magnonic information transfer in all spatial directions. We explicitly simulate hinge magnons in the presence of disorder and perturbations that break crystalline symmetries, unveiling their remarkable topological robustness owed to their chirality. Nonetheless, their path in real space turns out to be highly tunable by a manipulation of the surface termination at the atomic level. Thus, our findings empower magnonics with the tools of higher-order topology, opening up new avenues to achieve the sought-after control of spin-wave propagation [30–32]. We propose to realize SOTMIs in designer materials. In particular, we predict that a van der Waals heterostructure of chromium trihalides (e.g., $CrBr_3$, CrI_3) and nonmetallic transition metal dichalcogenides support second-order topological magnon spectra with chiral hinge magnons.

II. SECOND-ORDER TOPOLOGICAL MAGNONS

A. Model

We consider a stack of honeycomb magnets with spins situated at the honeycomb's vertices, as indicated by spheres in Fig. 2(a). The interactions between these spins are comprised in the Hamiltonian

$$H = H_\parallel + H_\perp + H_\perp^\delta + H_Z. \quad (1)$$

Here, intralayer interactions $H_\parallel = \sum_l h_\parallel^{(l)}$ (l is the layer index), with

$$h_\parallel^{(l)} = -\frac{J}{2}\sum_{\langle ij \rangle} \mathbf{S}_i^{(l)} \cdot \mathbf{S}_j^{(l)} + \frac{(-1)^l D}{2}\sum_{\langle\langle ij \rangle\rangle} \nu_{ij}\hat{\mathbf{z}} \cdot \mathbf{S}_i^{(l)} \times \mathbf{S}_j^{(l)}, \quad (2)$$

include positive nearest-neighbor exchange interaction J that stabilizes ferromagnetic order. Upon a magnon expansion (see Appendix A) a single layer is found to feature two magnon branches, resembling the graphene band structure with Dirac cones. The latter acquire a topological mass gap [33] $\pm 6\sqrt{3}D/J$ (later referred to as "bulk gap") by next-nearest-neighbor Dzyaloshinskii-Moriya interaction [34,35] (DMI) D [green arrows in Fig. 2(a)]; $\hat{\mathbf{z}}$ is a unit vector along the z direction and $\nu_{ij} = \pm 1$, with $+ (-)$ for counterclockwise (clockwise) circulation. The topological nontriviality is captured by a nonzero winding number $w^{(l)} = (-1)^l \text{sgn}(mD)$ (see Appendix B). Here, $m = +1$ ($m = -1$) for the ferromagnetic ground state pointing along the positive (negative) z direction. Hence, a single layer exhibits chiral edge states, as indicated by yellow spheres in Fig. 2(b). From hereinafter, we consider $m = +1$.

The AA-stacked honeycomb layers are coupled by

$$H_\perp = -J_\perp \sum_l \sum_i \mathbf{S}_i^{(l)} \cdot \mathbf{S}_i^{(l+1)}, \quad (3)$$

with ferromagnetic interlayer exchange $J_\perp$ due to which magnons obtain a dispersion along the stacking direction. We assume that $J_\perp$ is sufficiently small such that the bulk gap due to D stays open, which is a reasonable assumption for layered structures [36]. Using the Brillouin zone convention in Fig. 3(a), a representative bulk magnon spectrum is shown in Fig. 3(b); notice the band gap between the lower and upper pair of bands.
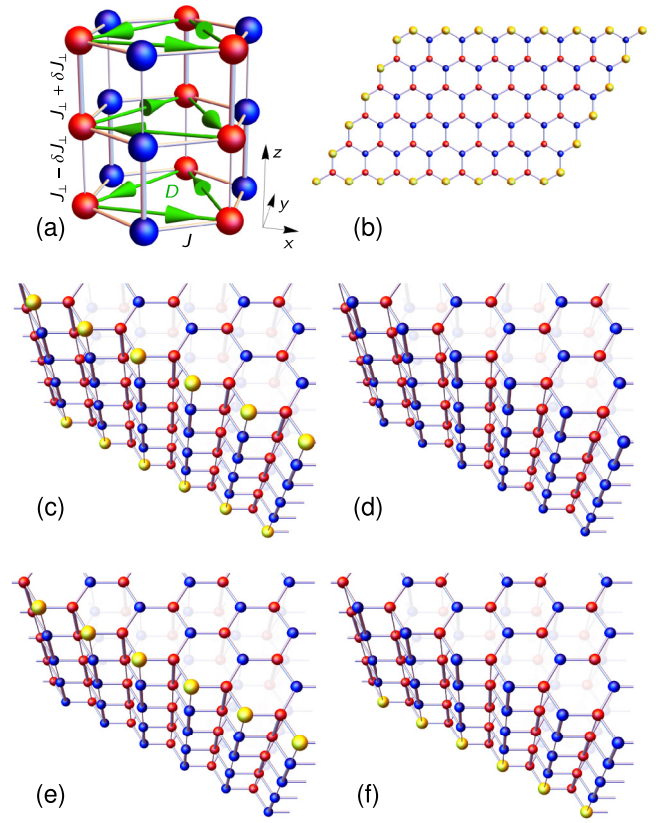

FIG. 2. Microscopic model of a SOTMI with chiral hinge states in three dimensions. (a) A stack of honeycomb layers with indicated magnetic interactions. Blue and red spheres indicate the A and B sublattices of the honeycomb, respectively. (b) A single honeycomb layer realizes a magnon Chern insulator, whose hallmark is a gap in the magnon spectrum bridged only by a chiral edge state (yellow spheres). (c)–(f) View along a zigzag-terminated surface of stacks built from a finite number of layers. Even-numbered stacks exhibit either (c) hinge modes at both terminating layers or (d) no hinge modes at all. In contrast, odd-layered stacks exhibit hinge states at one of the terminating layers, either at the top (e) or the bottom (f) of the stack.

Letting the sign of DMI alternate between adjacent layers ensures alternating winding numbers and chiral edge states, which gap out pairwise. However, since each layer is a mirror plane for the infinite stack, a magnonic surface Dirac cone is stabilized, rendering the surface spectrum gapless. Hence, so far, the stack is a (first-order) topological mirror insulator [37] of magnons (see Appendix C). To break this mirror symmetry, we effectively buckle each layer. This is accounted for by an alternating modulation of the interlayer exchange interaction ($\delta J_\perp$),

$$H_\perp^\delta = \delta J_\perp \sum_l (-1)^l \left(\sum_{i \in A} \mathbf{S}_i^{(l)} \cdot \mathbf{S}_i^{(l+1)} - \sum_{i \in B} \mathbf{S}_i^{(l)} \cdot \mathbf{S}_i^{(l+1)} \right), \quad (4)$$

which is opposite for the A and B sublattices of the honeycomb [cf. alternating interlayer bonds between blue and red sites in Fig. 2(a)]. Finally, a magnetic field $B^z < 0$ ($m = +1$)
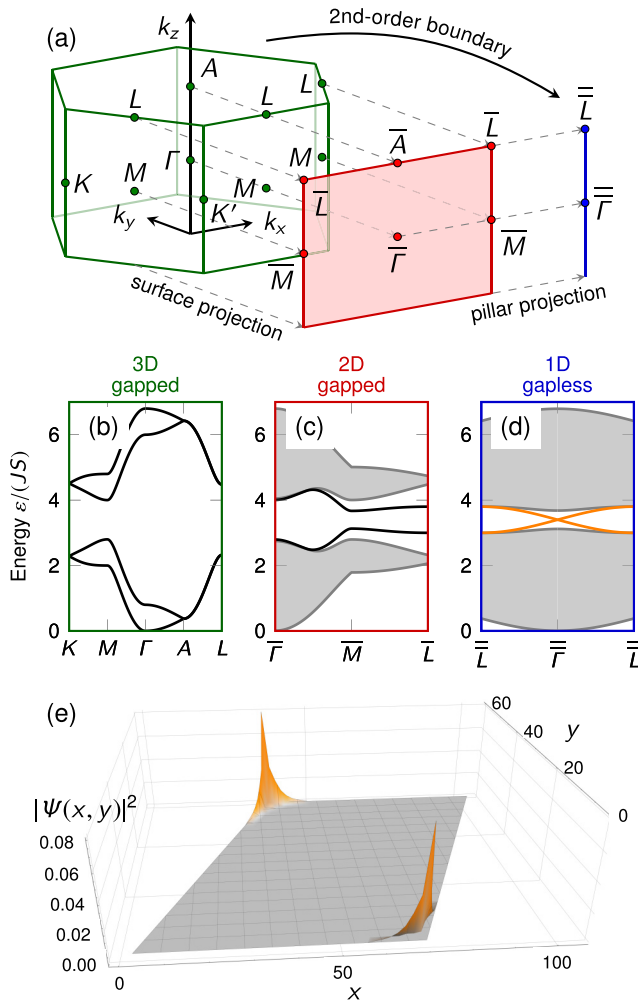
FIG. 3. Brillouin zones (BZs) and magnon band structures in 3D, 2D, and 1D. (a) For a successive reduction of dimensions, the hexagonal 3D BZ (green) first gets projected onto a surface to yield the 2D BZ (red), which then is projected onto a line, resulting in a 1D BZ (blue). Selected high-symmetry points are indicated. (b) Gapped 3D spectrum showing four magnon branches. (c) Gapped 2D spectrum, with gray areas indicating the bulk continuum projected onto the xz surface and black lines indicating surface states. (d) Gapless 1D spectrum with chiral hinge magnons crossing the band gap (orange lines). Gray areas indicate both the bulk and surface continuum projected onto the z axis. (e) Probability density $|\Psi(x, y)|^2$ of the chiral hinge-magnon states in real space for a pillar with a parallelogram cross section [cf. Fig. 2(b)] at $\overline{\overline{\Gamma}}$. Open boundary conditions are assumed in both x and y directions but periodic boundary conditions in the z direction. The two chiral modes are localized at opposite obtuse corners of the pillar. Parameters read as $d = j_\perp = \delta j_\perp = 0.2$ and $b = 0$.

is applied that enters the Zeeman Hamiltonian

$$H_Z = \sum_l \sum_i B^z S_i^{(l),z}. \quad (5)$$

The field is measured in units of energy. Using reduced constants $b = B^z/(JS)$, $j_\perp = J_\perp/J$, $d = D/J$, and $\delta j_\perp = \delta J_\perp/J$, the ferromagnetic ground state is stable for $|\delta j_\perp| \leqslant \frac{1}{2}\sqrt{(-b + 2j_\perp)(-b + 2j_\perp + 6)}$; note that $b \leqslant 0$. Below, we

consider parameters $d = j_\perp = \delta j_\perp = 0.2$, for which the ferromagnetic state is stable even at $b = 0$.

B. Gapless hinge magnons along domain walls

The mirror-symmetry breaking $\delta j_\perp$ acts like a mass that gaps out surface states, as depicted in Fig. 3(c). This can be understood in the following intuitive way. It is well established that the wave function of edge states in graphene has weight predominantly on the sublattice whose atoms dominate in a particular termination [38]. For example, the edge states of zigzag-terminated graphene live on that sublattice whose atoms constitute the very edge. Now, consider a stack of an even number of layers with a zigzag-terminated surface, as shown in Fig. 2(c). The surface state has weight mainly on the blue sublattice. Along the stacking direction, spins located at the blue sites of the chains resemble a spin version of the Su-Schrieffer-Heeger (SSH) model [39]. The sign of $\delta j_\perp$ determines whether the chain is topologically trivial or nontrivial, i.e., if its ends feature bound states [Fig. 2(c), $\delta j_\perp > 0$] or not [Fig. 2(d), $\delta j_\perp < 0$]. For an odd number of honeycomb layers, there is always one undimerized dangling spin hosting the bound state, either at the top [Fig. 2(e), $\delta j_\perp > 0$] or bottom layer [Fig. 2(f), $\delta j_\perp < 0$]. Due to the intralayer coupling of SSH-type chains, the states bound to the chains' ends can propagate along the hinge to which they are confined. The DMI-induced chirality of each layer admits propagation only in one direction, promoting the end states to chiral hinge modes.

A different surface of a finite stack may be terminated by the red sublattice that exhibits the opposite dimerization pattern. Hence, whatever sign of $\delta j_\perp$ causes bound states at a particular end of the blue chains leads to the red chains not hosting bound states at this very end (and vice versa). If domains of opposite surface terminations (of "opposite color") meet, there is a domain wall between a topologically trivial and nontrivial phase, necessitating a gapless mode along the domain wall, i.e., along the stacking direction. Such domain walls naturally occur at the hinges of materials where facets intersect, suggesting the name "chiral hinge magnons." In the spectrum of an infinite pillar (i.e., an infinite stack of honeycomb layers of finite size), hinge magnons appear as bands that connect adjacent bulk and surface bands, as shown in Fig. 3(d). The hinge-magnon wave function is strongly localized to the hinges [cf. Fig. 3(e)].

We present selected examples in Fig. 4. For a stack with a parallelogram cross section and all-zigzag termination, as shown in Fig. 4(a), the termination changes from blue to red at the obtuse corners. The associated hinges feature a domain wall and, hence, also a chiral hinge magnon, a prediction that is confirmed numerically by exact diagonalization of a finite sample by means of linear spin-wave theory [see Figs. 4(b) and 4(c)]. While the position of the hinge magnons is tied to the domain walls, it is the number of layers that determines the actual path taken. This is because a stack of an odd number of layers has a nonzero net winding number, originating from one layer being uncompensated [40]. Hence, there must be one chiral mode circulating the stack about the stacking direction [cf. Fig. 4(b)]. In contrast, an even number of layers has a net winding number of zero, ruling out any net
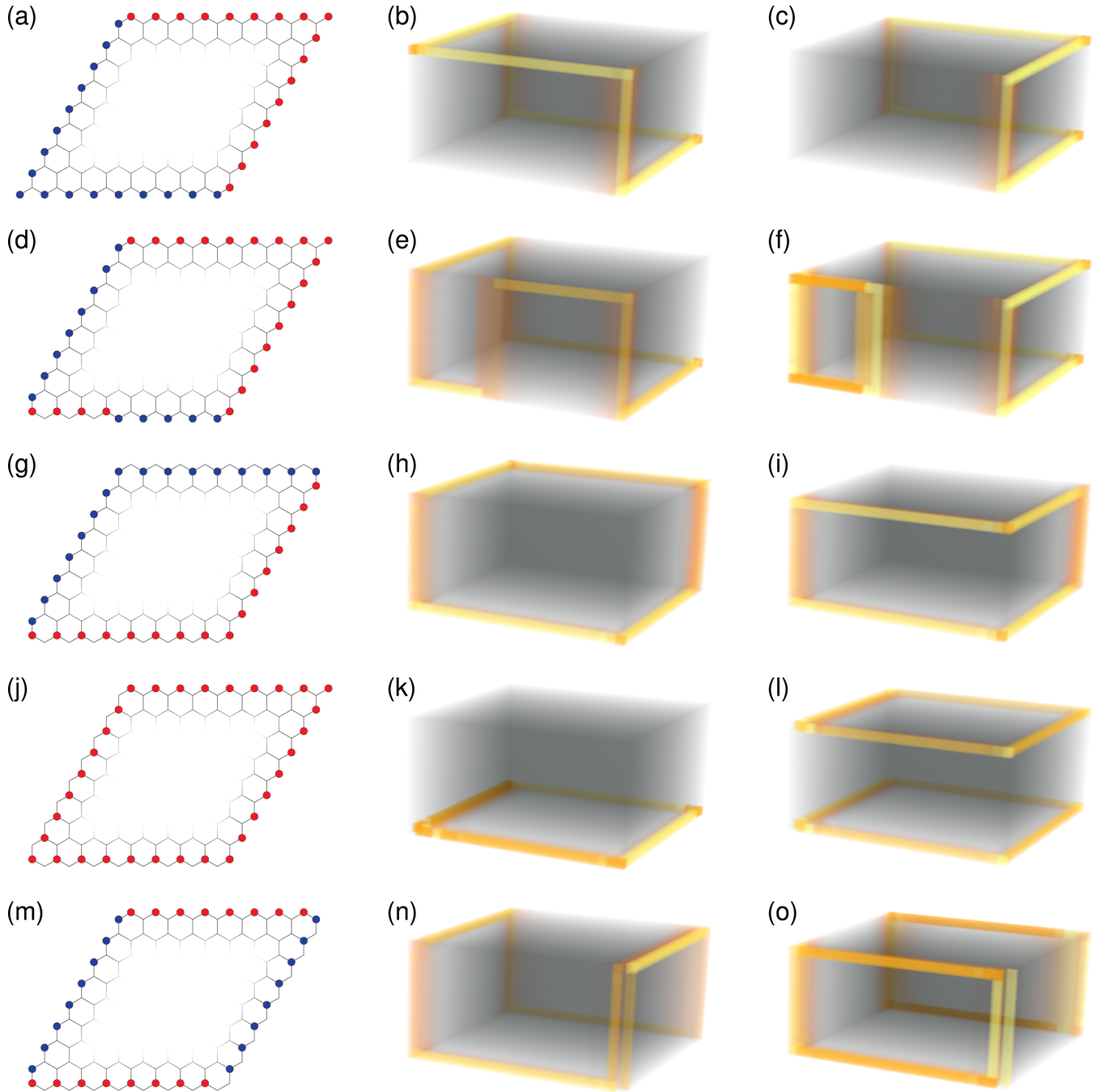
FIG. 4. Chiral hinge magnons in finite-sized stacks of honeycomb-lattice ferromagnets for selected terminations. (Left column) Sketch of stacks' cross sections with blue and red circles indicating the termination spanning the full height of the stack. (Central and right columns) Probability density of hinge magnons in a finite stack built from an odd (13) and even (12) number of layers. Each layer consists of 25×25 honeycomb unit cells. Black transparent (orange opaque) color indicates zero (maximal) probability density of the hinge magnon. The view angle is chosen such that the frontmost hinge coincides with the lower right corner of the cross sections. (a)–(c) All-zigzag terminated cross section with domain walls at the obtuse corners of the parallelogram. (d)–(f) Cross section with several blue vertical chains removed, giving rise to a new termination domain and, hence, two new domain walls. (g)–(i) Upon removing all terminating sites at two opposite boundaries, the domain walls get shifted to the acute corners. (j)–(l) Removing only the blue sites [compared to (a)] causes a uniform termination without domain walls. (m)–(o) Removing the terminating sites from the surfaces enclosing the frontmost obtuse corner [compared to (a)] causes domain walls at all hinges. Parameters read as $d = j_\perp = \delta j_\perp = 0.2$ and $b = 0$.

chirality about the stacking direction [cf. Fig. 4(c)]. Nonetheless, the hinge magnons are still chiral as their propagation is unidirectional.

Upon removing a couple of vertical blue chains from a surface, a red domain arises within the formerly blue-terminated surfaces [Fig. 4(d)]. Two new mass domain walls are created,

forcing the hinge magnon to take a detour in stacks with an odd number of layers [Fig. 4(e)]. For an even number of layers, two independent chiral hinge magnons, amounting to two separate loops, are found [Fig. 4(f)].

Removing all terminating spins from two opposite surfaces, as depicted in Fig. 4(g), results in the domain walls being shifted to the acute corners. The hinge magnons redistribute accordingly [see Figs. 4(h) and 4(i)]. Hence, termination manipulations at the atomic level allow to engineer samples with hinge modes at arbitrary hinges. In particular, one may remove any domain walls [Fig. 4(j)], resulting in the chiral modes not crossing the stack at all [Figs. 4(k) and 4(l)]. Similarly, domain walls at all hinges [Fig. 4(m)] cause chiral hinge magnons at all hinges [Figs. 4(n) and 4(o)]. We reiterate that the path of the hinge magnons depends also on the sign of $\delta j_\perp$, as we explicitly show in Appendix D.

For the very special case that the Hamiltonian respects inversion symmetry, the existence of chiral hinge magnons is captured by the recently developed machinery of higher-order topology [24–26], which associates a bulk topological number with the hinge modes. We show in Appendix E how to apply these tools to the present magnonic case but point out that inversion symmetry is not a prerequisite for chiral hinge magnons. As a matter of fact, Appendix F demonstrates that the chiral hinge magnons are remarkably robust against various types of inversion-symmetry-breaking bulk spin interactions.

C. Spin dynamics simulations of chiral hinge magnons

The above analysis relied on the magnon wave function as obtained within linear spin-wave theory. Next, we present independent numerical evidence for chiral hinge magnons by simulating a coherent excitation experiment by means of atomistic spin dynamics simulations based on the Landau-Lifshitz equation (see Appendix G 1 for technical details).

We consider a stack similar to that in Figs. 4(a)–4(c). An ac magnetic field with an energy $\varepsilon_{\mathrm{ex}} = 3.4JS$ within the global band gap [where the hinge magnons cross the $\overline{\overline{\Gamma}}$ point in Fig. 3(d)] applied to a single spin at the obtuse hinges excites the hinge magnon. Its chiral information transfer along the three-dimensional (3D) path can be clearly traced both for an odd number of layers [Fig. 5(a)] as well as for an even number of layers [Fig. 5(b)]. In contrast, a local excitation at the acute hinges does not result in chiral information transfer, but rather in an evanescent wave [Fig. 5(c)]. This finding complies with the absence of probability density of the chiral in-gap states at the acute corners [cf. Figs. 3(e), 4(b), and 4(c)].

The simulations also reveal the hinge magnon's robustness against backscattering at defects. We model the defect by locally applying large magnetic fields (along the z direction) to a selection of hinge spins and their neighbors, such that a spin wave has to pay a large potential energy penalty for crossing this area. We find that the chiral hinge mode simply bypasses the defect [Fig. 5(d)]. For the hinge magnon to scatter into states with opposite momentum, it would have to scatter to the opposite hinge, a process that is exponentially suppressed by spatial separation. Hence, chiral magnon information transfer is immune to defects. For movies of the snapshots shown in Fig. 5, see Supplemental Material, videos 1-4 [41].
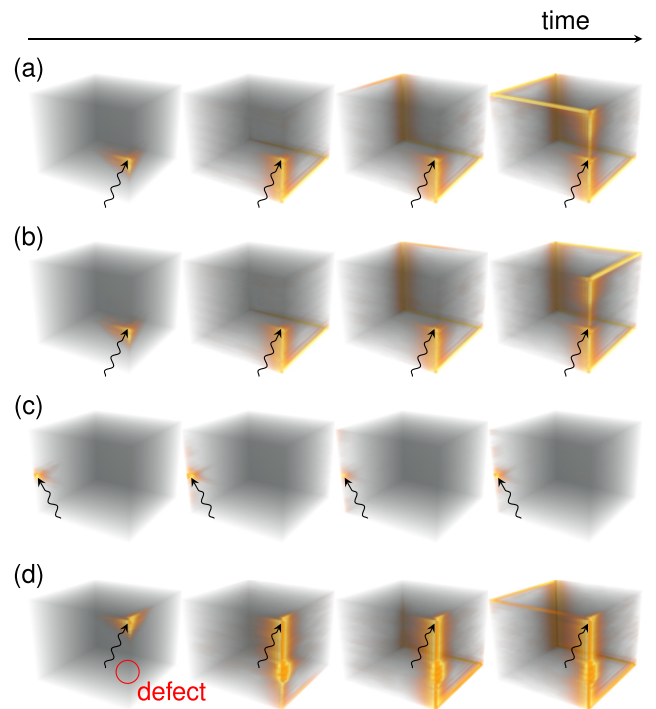

FIG. 5. Numerical simulation of a finite-sized SOTMI built from (a), (c), (d) 31 or (b) 30 layers. There are 40×40 honeycomb unit cells per layer. Snapshots show the time evolution upon a local coherent excitation (indicated by the wavy arrow) with an energy within the global band gap of the magnon spectrum [cf. Fig. 3(d)]. Black transparent (orange opaque) color indicates zero (maximal) probability density. (a) Upon exciting a single spin at a domain wall a topologically protected chiral magnon propagates around the sample along the hinges. (b) For an even number of layers, a similar excitation causes the hinge magnon to take a different path around the sample. (c) Excitations at hinges without a domain wall merely cause evanescent waves. (d) Due to the impossibility of backscattering the chiral excitation bypasses defects at the hinges. For movies, see Supplemental Material, videos 1–4 [41]: (a) SuppMov1.mov, (b) SuppMov2.mov, (c) SuppMov3.mov, and (d) SuppMov4.mov. The simulations are based on the Landau-Lifshitz equation without damping. Parameters read as $d = j_\perp = \delta j_\perp = 0.2$ and $b = 0$.

D. Robustness of chiral hinge magnons against disorder

The hinge magnons' localization to domain walls may be quantified by a localization length ξ, which is inversely proportional to the surface gap $\Delta \propto \delta j_\perp$ from broken mirror symmetry, thus, $\xi \propto 1/\delta j_\perp$. For large enough domains, of size $\ell \gg \xi$, neighboring counterpropagating hinge magnons are well separated and do not hybridize. However, if the boundary consists of domains $\ell \approx \xi$, hinge states of opposite chirality overlap and gap out. For example, consider the situation in Fig. 4(d) as a gradual process parametrized by $\lambda \in [0, 1]$. Starting with no vertical chains removed ($\lambda = 0$), one chain at a time is removed, until the termination of the manipulated surface has fully changed from zigzag (blue) to bearded (red) ($\lambda = 1$). Figure 6(a) shows the magnon spectrum of an infinite stack at the $\overline{\overline{\Gamma}}$ point [where the hinge modes cross, cf. Fig. 3(d)] in dependence on λ. Two degenerate states are found at $3.4JS$ (green line) corresponding to well-separated
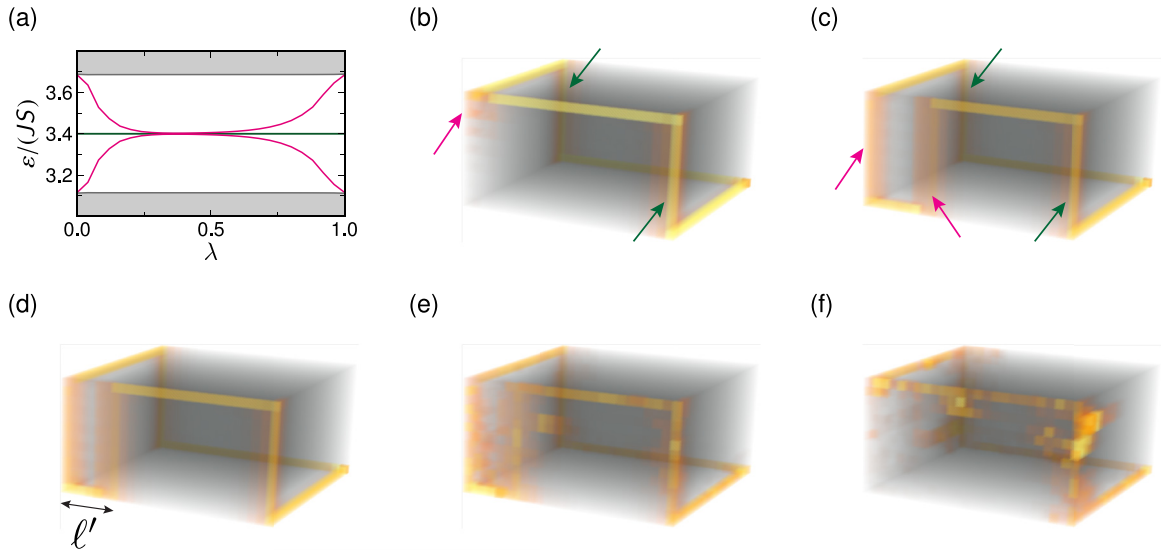
FIG. 6. Finite-size and disorder effects on chiral hinge magnons in SOTMIs. (a) Gapless 1D spectrum of an infinite stack at the $\overline{\overline{\Gamma}}$ point in dependence on λ which parametrizes the process of removing terminating vertical chains from one surface, a process similar to Fig. 4(d). $\lambda = 0$: no chains removed [blue termination in Fig. 4(d)]. $\lambda = 1$: all chains removed (red termination). Spatially well-separated hinge magnons appear as a green horizontal line. Two new hinge states associated with the new domain walls are colored in magenta. The gray continuum indicates projected bulk and surface states. (b), (c) Probability density of the hinge magnon in a finite stack of an odd number (13) of layers for (b) $\lambda \approx 0.12$ and (c) $\lambda \approx 0.32$. (d)–(f) Probability density of the hinge magnon for $\lambda \approx 0.24$ and increasing disorder; (d) $\sigma_b/\Delta = 0$; (e) $\sigma_b/\Delta = 1.11$; (f) $\sigma_b/\Delta = 1.48$. The hinge modes due to short domains (ℓ') gap out for sufficiently large disorder. Parameters read as $d = j_\perp = \delta j_\perp = 0.2$ and $b = 0$ and the pillar's cross section is built from 25×25 honeycomb unit cells per layer.

hinge modes [green arrows in Fig. 6(b)]. The surface gap hosts two states that split off for λ close to 0 or 1 [magenta lines in Fig. 6(a)]. In these limits, two domain walls come close together, causing their hinge magnons to overlap and gap out [magenta arrow in Fig. 6(b)]. However, around $\lambda = 0.5$, the domain sizes are sufficiently large to suppress finite-size effects and to enforce the chiral magnon to take a detour, as depicted in Fig. 6(c). Thus, it is ξ (or Δ) what sets the lower threshold for miniaturization of devices to support chiral hinge magnons.

The size of the gap Δ also protects the chiral hinge magnons against disorder, whose strength we denote by σ_b.[1] For example, Fig. 6(d) shows the probability density of a hinge magnon in the absence of disorder. The hinge magnon takes a detour around a small domain of length $\ell' > \xi$. As disorder is increasing, the effective, disorder-averaged gap $\Delta(\sigma_b)$ is decreasing, leading to an increasing $\xi(\sigma_b)$ [see Fig. 6(e)]. Once $\xi(\sigma_b) \gtrsim \ell'$ the associated hinge magnons gap out [see Fig. 6(f)]. Consequently, the hinge magnons of larger domains are more robust against disorder than those of smaller domains. Eventually, very strong disorder closes the gap and causes localization. The effects of disorder are also captured by spin dynamics simulations, presented in Appendix G 2 (for movies, see Supplemental Material, videos 5–9 [41]).

---

[1]We add random magnetic fields b_i^z, drawn from a uniform distribution $[-\frac{\beta}{2}, \frac{\beta}{2}]$, to all spins. Within linear spin-wave theory, the b_i^z's enter the main diagonal of the Hamilton matrix, resembling chemical-potential disorder known from electronic disorder studies. The disorder strength is measured by its standard deviation $\sigma_b = \beta/(2\sqrt{3})$.

III. EXPERIMENTAL REALIZATION IN VAN DER WAALS HETEROSTRUCTURES

As a specific example, we propose to realize the SOTMI phase in designer materials, in particular, in van der Waals (vdW) heterostructures that can be engineered with atomic precision [42] and allow for monolayer magnetism [43]. Magnetic vdW layers are no exception to the extraordinary control achieved by exfoliation [44,45] or growth through molecular beam epitaxy [46]. In particular, we point out that heterostructures of magnetic and nonmagnetic layers have already been synthesized [47,48]. Below, we take inspiration from these impressive experimental results to construct a SOTMI vdW heterostructure step by step.

So far, we considered stacks of layers with alternating DMI. However, this restriction can be relaxed. Let us denote the DMI of one layer by D and that of the neighboring layers by D'. Without loss of generality, let $D > 0$. For $D' = -D$, we recover Hamiltonian (1) and the SOTMI phase discussed above. However, for $D' = D$, each layer has the same winding number and all edge states have the same chirality. Hence, the chiral states do not gap out and the stack is a first-order topological (thick) Chern insulator. The phase transition between the two phases is associated with a bulk band-gap closing. Importantly, due to the interlayer coupling $J_\perp$, this closing does not happen at $D' = 0$ but at the nonzero critical value

$$D'_{\text{crit}} = \frac{4}{27} \frac{J_\perp^2}{D} > 0, \tag{6}$$

along vertical lines in reciprocal space passing through the K and K' points. The SOTMI phase is stable as long as $D' < D'_{\text{crit}}$, in particular, for $D' = 0$. This opens up the possibility

to realize a SOTMI by alternatingly stacking layers with and without DMI.

There is plenty of experimental and theoretical evidence that ferromagnetic monolayers of CrI$_3$ are magnonic Chern insulators. In particular, inelastic neutron scattering on bulk CrI$_3$ uncovered a bulk band gap within the honeycomb planes [49,50] and the spin susceptibility of an itinerant fermion description with parameters extracted from density functional theory revealed a topological gap with chiral edge states in a CrI$_3$ monolayer [51]. Within an effective spin model, both second-nearest-neighbor DMI D as well as Kitaev interaction open a topologically nontrivial gap [22,52–56].

Other representatives of the family of chromium trihalides, in particular CrBr$_3$, exhibit negligible spin-orbit coupling, as supported by both *ab initio* calculations [57] as well as neutron scattering [58]. Within the spirit of our model, they represent suitable $D' = 0$ layers. Between the lattice constants of CrBr$_3$ (6.45 Å) and CrI$_3$ (6.97 Å) there is a relative mismatch of about 8% [59]. However, the CrI$_3$ layers may be replaced with their Janus monolayer relative Cr(I,Br)$_3$ with a lattice constant 6.47 Å [53], reducing the mismatch to below half a percent.

Heterostructures with a designer unit cell CrBr$_3$/Cr(I,Br)$_3$ already realize one of the most important ingredients: an alternation between zero and nonzero DMI that allows for the SOTMI phase as explained above. However, such heterostructures miss the dimerization pattern of the interlayer coupling ($\delta J_\perp = 0$) and are only first-order topological, as considered in Ref. [60]. To design such dimerization, we propose to use intermediate nonmetallic transition metal dichalcogenide (TMD) layers. Several of these TMDs come with a lattice constant that is almost half of that of the chromium trihalides, examples are MoTe$_2$ (3.5 Å), HfS$_2$ (3.6 Å), and WSe$_2$ (3.3 Å) [61]. Hence, the TMD layer can be arranged in several Cr-sublattices asymmetric setups, as explored in Ref. [61] (and experimentally realized for MoSe$_2$ on top of CrBr$_3$ [48]): either the metal atom, the chalcogen atom, or a vacancy is on top of the Cr atoms. *Ab initio* calculations suggest that the arrangement with chalcogen atoms on top of Cr atoms is the most stable [61], as indicated in Fig. 7(a). The crucial idea is now to flip every second TMD layer upside down, resulting in the chalcogen atom to be located on top of the other Cr atom [cf. Fig. 7(b)]. This alternating arrangement of intermediate TMD layers results in a dimerization pattern of the interlayer paths between Cr atoms [cf. Fig. 7(c)] that also causes a dimerization of the interlayer exchange coupling ($\delta J_\perp \neq 0$).

In conclusion, we propose to realize a SOTMI in vdW heterostructures with the designer unit cell TMD′/CrBr$_3$/TMD/Cr(I,Br)$_3$, where the prime distinguishes the two configurations in Figs. 7(a) and 7(b). In the following, we study the magnon topology of such a stack by means of an effective magnetic Hamiltonian, with magnetic interaction parameters either taken from experiments or *ab initio* calculations. The influence of the TMD layers is effectively accounted for in the coupling between the chromium trihalide layers. Thus, we arrive again at a spin Hamiltonian with spins situated at AA-stacked honeycomb layers, as depicted in Fig. 7(d). We write the effective spin Hamiltonian $H = \sum_u H^{(u)}$ as a sum over unit-cell
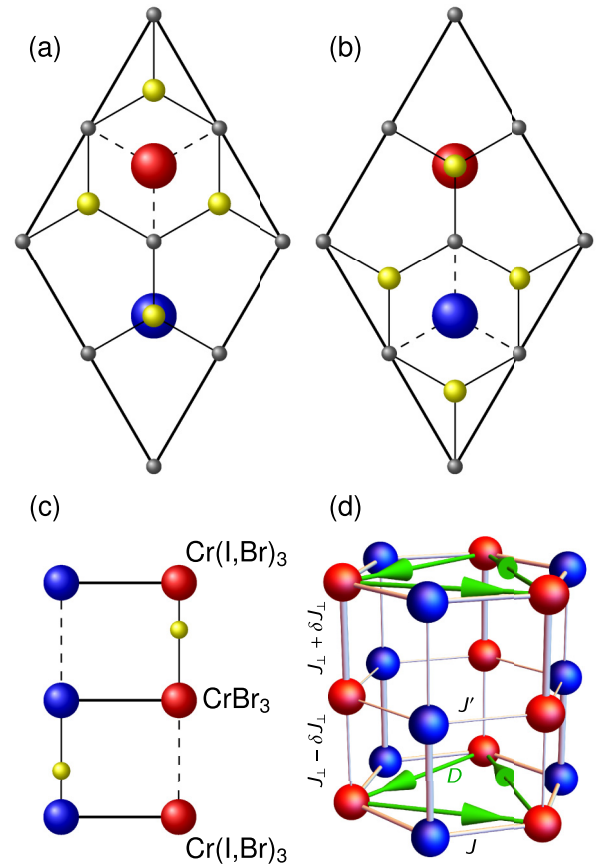

FIG. 7. Real-space construction of a SOTMI in a vdW heterostructure built from chromium trihalides layers and TMD layers. Blue (red) spheres indicate the Cr atoms of the chromium trihalides layers on the A (B) sublattice of the honeycomb lattice. Br and I atoms are not indicated. Gray (yellow) spheres indicate the metal (chalcogen) atoms of the TMD layer. The lattice constant of the TMD layers is half of that of the chromium trihalides layers. (a) TMD layer on top of Cr(I,Br)$_3$, with the chalcogen atom on top of the blue Cr sublattice. (b) Flipped TMD layer on top of CrBr$_3$, with the chalcogen atom on top of the red Cr sublattice. (c) Vertical view of the vdW stack, with chalcogen atoms causing a dimerization pattern, as indicated by dashed and solid lines. Metal atoms are not indicated. (d) Effective magnetic model of the vdW layer stack, with magnetic interactions indicated. In contrast to Fig. 2(a), the intralayer Heisenberg exchange interactions (J and J') are different, the DMI of every second layer is zero, and there is magnetic anisotropy A in layers with nonzero DMI.

Hamiltonians

$$H^{(u)} = H^{(u)}_{\mathrm{Cr(I,Br)_3}} + H^{(u)}_{\mathrm{CrBr_3}} + H^{(u)}_{\mathrm{Cr(I,Br)_3 \to CrBr_3}}$$
$$+ H^{(u)}_{\mathrm{CrBr_3 \to Cr(I,Br)_3}}, \tag{7}$$

which themselves are composed from sub-Hamiltonians $H^{(u)}_{\mathrm{Cr(I,Br)_3}}$, $H^{(u)}_{\mathrm{CrBr_3}}$, $H^{(u)}_{\mathrm{Cr(I,Br)_3 \to CrBr_3}}$, and $H^{(u)}_{\mathrm{CrBr_3 \to Cr(I,Br)_3}}$ that, respectively, describe the magnetic interactions within the Cr(I,Br)$_3$ and CrBr$_3$ layers, and between them. The spin quantum number is $S = \frac{3}{2}$ for all layers.

We model the $Cr(I,Br)_3$ layers by

$$H_{Cr(I,Br)_3}^{(u)} = -\frac{J}{2}\sum_{\langle ij\rangle} S_i^{(u)} \cdot S_j^{(u)} + \frac{D}{2}\sum_{\langle\langle ij\rangle\rangle} \nu_{ij}\hat{z} \cdot S_i^{(u)} \times S_j^{(u)}$$
$$- A\sum_i \left(S_{i,z}^{(u)}\right)^2, \qquad (8)$$

with $J = 1.8$ meV, $D = 0.07$ meV, and anisotropy $A = 0.12$ meV, as obtained from density functional theory [53]. The summations in Eq. (8) are to be understood over those spins $S_i^{(u)}$ in the $Cr(I,Br)_3$ layer of the uth unit cell. The lowest honeycomb layer in Fig. 7(d) represents a $Cr(I,Br)_3$ layer.

Some comments are due on those magnetic interactions in $Cr(I,Br)_3$ that we have neglected. First, we have neglected further-neighbor Heisenberg exchange because of their subdominant influence on the spectrum. Second, we have neglected the Kitaev interaction in $Cr(I,Br)_3$ [53] and attributed the topological gap entirely to the second-nearest-neighbor DMI. We point out that the specific origin of the topological gap is not important to our proposal. Third, Janus monolayers break inversion symmetry. As already shown, this is not detrimental to the existence of chiral hinge magnons but it allows for considerable in-plane DMI interaction that favors noncollinear spin structures such as spin spirals or skyrmions [53,62,63]. However, this tendency to spiralization can be easily overcome by an external magnetic field. Consequently, we neglect in-plane DMI altogether due to its subleading influence on the magnon spectrum [64]. Fourth, out-of-plane nearest-neighbor DMI [52] is neglected because it does not open a topological gap.

As for the $CrBr_3$ layer, neutron scattering data suggest that it is very well modeled by

$$H_{CrBr_3}^{(u)} = -\frac{J'}{2}\sum_{\langle ij\rangle} S_i^{(u)} \cdot S_j^{(u)} + \frac{D'}{2}\sum_{\langle\langle ij\rangle\rangle} \nu_{ij}\hat{z} \cdot S_i^{(u)} \times S_j^{(u)}, \quad (9)$$

with nearest-neighbor Heisenberg exchange $J' = 1.56$ meV only [58]. The absence of an experimentally resolvable topological magnon gap in $CrBr_3$ implies $D' = 0$, as indicated by the absence of green arrows in the middle honeycomb layer in Fig. 7(d).

For the coupling between the layers, we make the ansatz

$$H_{Cr(I,Br)_3 \to CrBr_3}^{(u)} = -(J_\perp + \delta J_\perp)\sum_{i\in A}\sum_{j\in A} S_i^{(u)} \cdot S_j^{(u)}$$
$$- (J_\perp - \delta J_\perp)\sum_{i\in B}\sum_{j\in B} S_i^{(u)} \cdot S_j^{(u)}, \quad (10)$$

where i (j) runs over spins in the $Cr(I,Br)_3$ ($CrBr_3$) layer of the same unit cell. Similarly,

$$H_{CrBr_3 \to Cr(I,Br)_3}^{(u)} = -(J_\perp - \delta J_\perp)\sum_{i\in A}\sum_{j\in A} S_i^{(u)} \cdot S_j^{(u+1)}$$
$$- (J_\perp + \delta J_\perp)\sum_{i\in B}\sum_{j\in B} S_i^{(u)} \cdot S_j^{(u+1)}, \quad (11)$$

where i (j) runs over spins in the $CrBr_3$ [$Cr(I,Br)_3$] layer of neighboring unit cells. This results in the effective dimerization pattern depicted in Fig. 7(d). In the absence of exact values, we have to estimate the interlayer exchange coupling
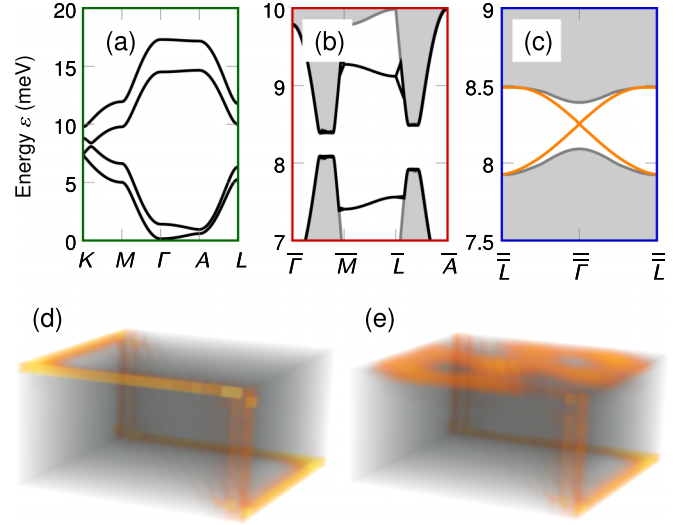

FIG. 8. Second-order topological magnons in a vdW heterostructure with the designer unit cell $TMD'/CrBr_3/TMD/Cr(I,Br)_3$. (a)–(c) Magnon spectra along high-symmetry lines. For the definition of high-symmetry points, see Fig. 3(a). (a) Gapped bulk magnon spectrum. (b) Gapped zigzag-surface magnon spectrum, with black lines indicating surface states and gray continua the projection of the bulk bands. (c) Gapless pillar magnon spectrum, with orange lines indicating chiral hinge modes and gray continua the projection of bulk and surface states. The pillar cross section is all-zigzag terminated, as in Fig. 4(a). (d), (e) Probability density of hinge magnons in a finite stack. Each layer consists of 25×25 honeycomb unit cells. Black transparent (orange opaque) color indicates zero (maximal) probability density of the hinge magnon. (d) A stack built from 13 layers, with both the top and bottom terminating layers being $Cr(I,Br)_3$. (e) Stack built from 12 layers, with the top terminating layer being $CrBr_3$ and $Cr(I,Br)_3$ for the bottom terminating layer. Parameters read as $J = 1.8$ meV, $D = 0.07$ meV, $J' = 1.56$ meV, $D' = 0.00$ meV, $A = 0.12$ meV, $J_\perp = 0.2$ meV, $\delta J_\perp = 0.1$ meV, and $S = \frac{3}{2}$.

$J_\perp$. From neutron scattering data it was extracted that the interlayer coupling in bulk CrI_3 is about four times smaller than the intralayer coupling [49]. In our stack, due to the intermediate TMD layers, the interlayer coupling is expected to be smaller. We set $J_\perp = 0.2$ meV but note that the actual value is not crucial; the ferromagnetic SOTMI phase is stable as long as

$$0 < J_\perp < \frac{\sqrt{JJ'(2J + A - J')(2J' - J - A)}}{J + J'} \approx 0.8 \text{ meV}. \quad (12)$$

Even if $J_\perp$ was antiferromagnetic, an external magnetic field could overcome the energy for both a spin-flop transition and field polarization. Finally, for the dimerization, we take $\delta J_\perp = 0.1$ meV. Again, the exact value is not important for magnon topology; any nonzero $\delta J_\perp$ gaps out the surface states.

We proceed with a similar analysis as in Sec. II. The bulk, surface, and pillar magnon spectra of the vdW layer stack are depicted in Figs. 8(a)–8(c). The SOTMI phase is readily verified by noting that both the bulk and the surface spectrum are gapped but the pillar spectrum supports gapless chiral hinge states within the band gap.

Figures 8(d) and 8(e) show the probability density of the chiral hinge magnon for a finite stack built from an odd and even number of layers, respectively. For an odd number of layers, both the top and bottom terminating layer is $Cr(I,Br)_3$, i.e., layers with nonzero DMI. Consequently, the probability density of the chiral hinge magnon is well localized to the vertical as well as the horizontal hinges. In contrast, for an even number of layers, one of the terminating layers, the top one in Fig. 8(e), has to be $CrBr_3$, i.e., a layer with zero DMI. Since this layer is not sandwiched by $Cr(I,Br)_3$ layers, there is no mechanism to gap out its Dirac magnons. Hence, the top layer is gapless, causing the "hinge" magnon to spread out over the entire top layer. (For a stack with $CrBr_3$ for the top and bottom layer, the hinge magnon spreads over both the top and bottom layers). This finding is not in contradiction to the claim of nontrivial second-order topology; in the absence of DMI in the top layer, the hinge mode just hybridizes with a gapless surface state. However, to facilitate an experimental detection of chiral hinge magnons, it seems best to terminate the stack with a $Cr(I,Br)_3$ layer instead of a $CrBr_3$ layer. In any case, the hinge mode is strongly localized to the vertical hinges.

IV. DISCUSSION OF NONLINEARITIES

So far, our analysis of chiral hinge magnons relied on the harmonic approximation: we neglected magnon-magnon interactions in the calculation of the magnon spectra and used small excitation amplitudes in spin dynamics simulations. Here, we comment on the effects of magnon-magnon interactions and other nonlinearities to argue that second-order topological magnons are robust against many-body effects. In contrast to electrons, for which there is no small parameter to perturbatively include electron-electron interactions, magnons do allow for a perturbative analysis. The small parameter is $1/S$ or, effectively, temperature T in spin-wave theory and the spin vectors' deviation from the magnetization direction (i.e., their opening angle) in spin dynamics simulations.

A. Zero-temperature magnon lifetime

Although the influence of disorder and defects is suppressed by the topological gap, a finite lifetime of chiral hinge magnons can still originate from phononic or, in metals, electronic baths. For the nonmetallic stack under consideration, spontaneous decays due to inelastic magnon-phonon scattering cause a finite magnon lifetime, e.g., a magnon spontaneously decays into another magnon at lower energy under emission of a phonon. Similarly, magnetic interactions that break spin rotation symmetry and connect in-plane with out-of-plane spin components (e.g., $S^x S^z$) cause spontaneous magnon decay into two other magnons [65]. However, both effects should be small because to leading order (order $1/S$) they scale quadratically with the magnetoelastic coupling constant and magnetic interactions originating from spin-orbit coupling, respectively. (Enhancing effects due to van Hove singularities in the joint magnon-phonon or two-magnon density of states [66] can always be avoided by magnetic-field tuning). On top of that, at present, the influence of the chirality of a topologically protected edge mode on the respective scat-

tering vertices has not been studied in detail. In the absence of a detailed analysis, we model the finite magnon lifetime $\tau = \hbar/(\alpha\varepsilon)$ [67] by an intrinsic Gilbert damping α [68] that we assume to be smaller than that of bulk magnons, i.e., of the order $\alpha \in [10^{-5}, 10^{-4}]$. With the hinge magnons appearing approximately at an energy $\varepsilon = 8.2$ meV [cf. Fig. 8(c)], their lifetime is estimated as $\tau \in [0.8 \text{ ns}, 8 \text{ ns}]$. In spectral terms, this corresponds to a zero-temperature linewidth no larger than 1 μeV. The chiral hinge mode is well defined as long as its supporting spectral gap is larger than its linewidth, as is the case in Fig. 8(c).

B. Finite temperatures

When both magnetoelastic coupling and U(1) symmetry-breaking magnetic interactions are negligible, number-nonconserving interactions and spontaneous magnon decay are ruled out. Then, number-conserving four-magnon interactions become the leading-order many-body perturbation. They are frozen out at zero temperature but renormalize the magnon energy and damping at finite temperature [69]. At order $1/S$, four-magnon interactions cause a purely real renormalization that uniformly shifts the magnon energies downwards in energy. For a single honeycomb layer, this effect was already studied and found to scale with T^2 [70], with the exponent determined by the dimension of the magnet. Extending this analysis to three dimensions, we expect the scaling $T^{5/2}$. The uniform compression of the magnon spectrum leads to a reduction of the group velocities, implying that the chiral hinge magnons slow down as temperature increases. Complex self-energies appear first at order $1/S^2$ and describe additional magnon damping, which also scales with T^2 in two dimensions [70] and, hence, with $T^{5/2}$ in three dimensions. The stability of the chiral hinge modes is lifted when their temperature-induced lifetime broadening becomes as large as the spectral gap they cross. This condition defines a critical temperature T' below which chiral hinge magnons can be detected. The larger the spectral gap, the larger is T'.

The above considerations apply to the case of zero magnetic field and in the absence of easy-axis anisotropy. Both finite fields and easy-axis anisotropies shift the magnon spectrum uniformly towards higher energies, exponentially freezing out thermal effects due to a finite spin-wave gap. Hence, thermal effects can be systematically suppressed by external control or by an engineering of magnetic anisotropies by strain [71].

C. Large excitation amplitudes

For the spin dynamics simulations in Sec. II C, we used small excitation amplitudes, i.e., in-plane dynamic magnetic fields with amplitude $B_0 \ll J$. Then, the internal magnetic fields due to the exchange interaction are much larger than the external field and the spins are only slightly canted away from the ferromagnetic ground-state direction. In this limit, nonlinearities of the equation of motion are suppressed, facilitating the comparison with results obtained within the harmonic approximation.

Here, we compare the $B_0 \ll J$ limit with the opposite $B_0 \gg J$ limit, in which the excited spin almost completely
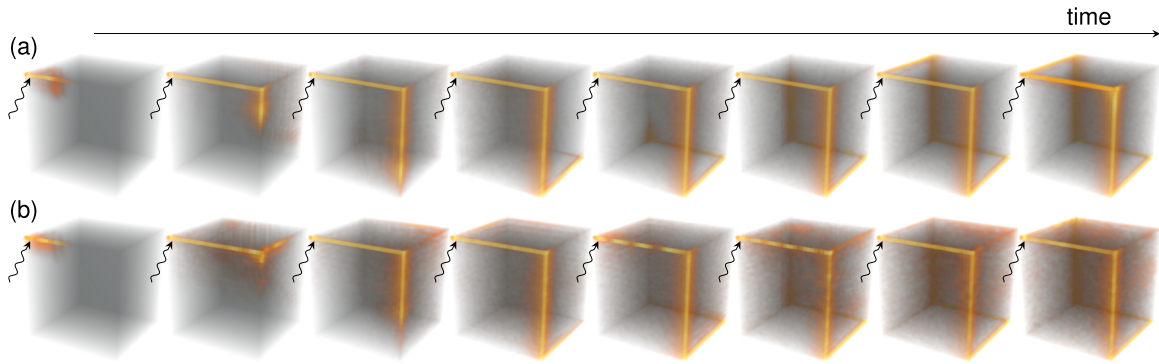
FIG. 9. Comparison of linear and nonlinear excitation of chiral hinge magnons in a finite-sized SOTMI. Snapshots show the time evolution upon a local coherent excitation (indicated by the wavy arrow) with an energy within the global band gap of the magnon spectrum. Black transparent (orange opaque) color indicates zero (maximal) probability density. (a) Excitation with a dynamic magnetic field the amplitude of which is much smaller than the exchange energy: $B_0 = 0.05J$. (b) Excitation with a dynamic magnetic field the amplitude of which is much larger than the exchange energy: $B_0 = 20J$. The magnetic interaction parameters are identical to those in Fig. 5.

aligns with the dynamic field. Hence, its opening angle is approximately $90°$ and the linear spin-wave approximation does not hold. Nonetheless, the results of spin dynamics simulations shown in Fig. 9 reveal very similar features for both $B_0 \ll J$ [Fig. 9(a)] and $B_0 \gg J$ [Fig. 9(b)]. The signal of the excited chiral hinge magnon is clearly visible and excellently compares with the results extracted from the linear theory. A direct comparison of snapshots at equal times reveals that the strongly excited chiral hinge magnon has a slightly smaller propagation velocity. We conclude that chiral hinge magnons and second-order magnon topology are remarkably robust against nonlinearities.

V. CHIRAL HINGE MAGNONS FOR MAGNONICS

The SOTMI realized in vdW heterostructures may find application in terahertz magnonics [72]. The group velocity of the chiral hinge magnon along the stacking direction is approximately $v = 400$ m/s, as extracted from Fig. 8(c) and assuming a spacing of 1 nm between magnetic layers. Thus, a chiral hinge magnon propagates $\ell = v\tau \in [0.32 \ \mu\text{m}, 3.2 \ \mu\text{m}]$ before decaying (τ is taken from Sec. IV A). It crosses several hundred vdW layers during its lifetime. To exploit the phase information of the chiral magnon, the ratio ℓ/λ, with $\lambda = 2\pi/k$ being the magnon wavelength, must be large [67]. Thus, according to Fig. 8(c), the excitation frequency must be chosen such that chiral modes at $k \neq 0$ are excited. For example, chiral hinge magnons at $k = 0.1 \ \text{nm}^{-1}$ have a wavelength $\lambda \approx 63$ nm. This corresponds to $\ell/\lambda \approx 50$ for an effective Gilbert damping $\alpha = 10^{-5}$ of chiral hinge magnons. Aside from the vdW layers platform, an atomistic SOTMI may also be realized by relying on recent advances in atomic-scale magnonic crystals [73] or magnetic organic materials [74].

Our design principle for magnonic SOTMIs can also be carried over to magnonic metamaterials for gigahertz magnonics where ratios $\ell/\lambda \approx 3000$ are typical [67]. In particular, one may stack two-dimensional topological magnonic crystals realized as (i) arrays of iron islands in an yttrium iron garnet matrix [5], (ii) arrays of ferromagnetic particles [75],

(iii) arrays of magnetic rings [76], (iv) hexagonally arranged triangular holes in patterned ferrimagnetic insulators [77], or (v) artificial spin-ice metamaterials [78,79]. The Chern numbers of volume-mode bands are, respectively, determined by (i) the aspect ratio of the islands, (ii), (iii) the external magnetic field, (iv) the orientation of the triangular holes, and (v) the sign of the effective coupling between islands constituting the spin ice. Within the description of Hamiltonian (1), layers with alternating Chern number have to be stacked in such a way that the stack exhibits no mirror symmetry in stacking direction. Such stacks will realize gigahertz hinge magnons with mean-free paths up to a millimeter. Using a similar design idea, SOTMIs can also be implemented in magnonic metamaterials built from three-dimensional coupled arrays of spin torque oscillators [80], magnetic vortex structures [81], magnonic quantum networks [82], or superconducting spin qubits [83].

VI. CONCLUSION

We introduced a topological phase of matter dubbed SOTMI to be realized either in magnetic metals or insulators. Its hallmarks are chiral magnon states along its hinges. We proposed to realize a SOTMI in van der Waals designer materials. We demonstrated that a heterostructure of magnetic and nonmagnetic vdW layers exhibits a second-order topological magnon spectrum and explicitly presented its chiral hinge magnons. We showed that chiral hinge magnons are remarkably robust against defects, disorder, periodic bulk perturbations that break specific crystalline symmetries, and nonlinearities, in particular, many-body perturbations both at zero and nonzero temperature. Aside from being an exotic second-order topological phase that could allow one to experimentally test the foundations of higher-order topology, chiral hinge magnons open up possibilities to design 3D magnonic "information highways," circumventing the problem of nontopological magnon propagation in bent magnonic waveguides [84]. Thus, SOTMIs are a promising candidate for 3D magnonics [85].

APPENDIX A: LINEAR SPIN-WAVE THEORY

The excitations above a magnetically ordered ground state can be addressed within spin-wave theory, whose main idea is to map the spin operators $\boldsymbol{S}_i$ onto bosonic creation and annihilation operators $a_i^\dagger$ and a_i. In the limit of low temperatures, within which the density of excitations is sufficiently small that interactions between them may be neglected, a truncated Holstein-Primakoff transformation [86]

$$S_i^x \approx \sqrt{\frac{S}{2}}(a_i + a_i^\dagger), \tag{A1a}$$

$$S_i^y \approx -\mathrm{i}\sqrt{\frac{S}{2}}(a_i - a_i^\dagger), \tag{A1b}$$

$$S_i^z = S - a_i^\dagger a_i \tag{A1c}$$

is appropriate; $\mathrm{i}^2 = -1$. For the model under consideration, there are four spins in the basis because the dimerization pattern due to $\delta J_\perp$ doubles the honeycomb unit cell in the

stacking direction. The bosonic operators may be labeled $a_{n,\boldsymbol{R}_i}$, where $\boldsymbol{R}_i$ is the coordinate vector of the ith magnetic basis and $n = 1, \ldots, 4$ enumerates the nth basis spin. After a Fourier transformation

$$a_{n,\boldsymbol{R}_i} = \frac{1}{\sqrt{N}}\sum_{i=1}^{N} e^{\mathrm{i}\boldsymbol{k}\cdot\boldsymbol{R}_i} a_{n,\boldsymbol{k}}, \tag{A2}$$

to momentum $\boldsymbol{k}$, where N is the number of unit cells, the Hamiltonian reads as $H - E_0 \approx H_2 = \sum_{\boldsymbol{k}} \boldsymbol{\Psi}_{\boldsymbol{k}}^\dagger \cdot \mathsf{H}_{\boldsymbol{k}} \cdot \boldsymbol{\Psi}_{\boldsymbol{k}}$. Here, E_0 is the unimportant classical ground-state energy and $\boldsymbol{\Psi}_{\boldsymbol{k}}^\mathrm{T} = (a_{1,\boldsymbol{k}}, a_{2,\boldsymbol{k}}, a_{3,\boldsymbol{k}}, a_{4,\boldsymbol{k}})$ a vector built from Holstein-Primakoff bosons associated with the four sublattices. The Fourier kernel of the bilinear Hamiltonian H_2 reads as

$$\mathsf{H}_{\boldsymbol{k}} = SJ\begin{pmatrix} \mathsf{H}_{\boldsymbol{k}}^{\|,+} & \mathsf{H}_{\boldsymbol{k}}^{\perp} \\ (\mathsf{H}_{\boldsymbol{k}}^{\perp})^* & \mathsf{H}_{\boldsymbol{k}}^{\|,-} \end{pmatrix}. \tag{A3}$$

The intralayer and interlayer submatrices of the Fourier kernel are given by

$$\mathsf{H}_{\boldsymbol{k}}^{\|,\pm} = (3 - b + 2j_\perp)\sigma_0 + \boldsymbol{h}_{\boldsymbol{k}}^{\|,\pm} \cdot \boldsymbol{\sigma}, \tag{A4a}$$

$$\mathsf{H}_{\boldsymbol{k}}^{\perp} = -(j_\perp^+ + j_\perp^- \cos k_z)\sigma_0 + \mathrm{i}j_\perp^- \sin k_z \sigma_3, \tag{A4b}$$

respectively. We used reduced parameters $b = B^z/(JS)$, $j_\perp = J_\perp/J$, $d = D/J$, and $\delta j_\perp = \delta J_\perp/J$, abbreviated $j_\perp^\pm = j_\perp \pm \delta j_\perp$, and introduced the Pauli matrices σ_0 (identity) and $\boldsymbol{\sigma} = (\sigma_1, \sigma_2, \sigma_3)$. Furthermore,

$$\boldsymbol{h}_{\boldsymbol{k}}^{\|,+} = \begin{pmatrix} -\cos[\boldsymbol{k}\cdot(-\boldsymbol{\tau}_2)] - \cos[\boldsymbol{k}\cdot\boldsymbol{\tau}_3] - \cos[\boldsymbol{k}\cdot(\boldsymbol{\tau}_3-\boldsymbol{\tau}_2)] \\ \sin[\boldsymbol{k}\cdot(-\boldsymbol{\tau}_2)] + \sin[\boldsymbol{k}\cdot\boldsymbol{\tau}_3] + \sin[\boldsymbol{k}\cdot(\boldsymbol{\tau}_3-\boldsymbol{\tau}_2)] \\ 2d\sum_{i=1}^{3}\sin(\boldsymbol{k}\cdot\boldsymbol{\tau}_i) \end{pmatrix}, \tag{A5}$$

and

$$\boldsymbol{h}_{\boldsymbol{k}}^{\|,-} = \begin{pmatrix} -\cos[\boldsymbol{k}\cdot(\boldsymbol{\lambda}-\boldsymbol{\tau}_2)] - \cos[\boldsymbol{k}\cdot(\boldsymbol{\lambda}+\boldsymbol{\tau}_3)] - \cos[\boldsymbol{k}\cdot(\boldsymbol{\lambda}+\boldsymbol{\tau}_3-\boldsymbol{\tau}_2)] \\ \sin[\boldsymbol{k}\cdot(\boldsymbol{\lambda}-\boldsymbol{\tau}_2)] + \sin[\boldsymbol{k}\cdot(\boldsymbol{\lambda}+\boldsymbol{\tau}_3)] + \sin[\boldsymbol{k}\cdot(\boldsymbol{\lambda}+\boldsymbol{\tau}_3-\boldsymbol{\tau}_2)] \\ -2d\sum_{i=1}^{3}\sin(\boldsymbol{k}\cdot\boldsymbol{\tau}_i) \end{pmatrix} \tag{A6}$$

with vectors

$$\boldsymbol{\tau}_1 = (\sqrt{3}, 0, 0), \tag{A7a}$$

$$\boldsymbol{\tau}_2 = (-\sqrt{3}/2, 3/2, 0), \tag{A7b}$$

$$\boldsymbol{\tau}_3 = (-\sqrt{3}/2, -3/2, 0), \tag{A7c}$$

$$\boldsymbol{\lambda} = (0, 0, 1). \tag{A7d}$$

The nearest-neighbor distance is set to one. The reason for $\boldsymbol{\lambda}$ only entering $\boldsymbol{h}_{\boldsymbol{k}}^{\|,-}$ and not $\boldsymbol{h}_{\boldsymbol{k}}^{\|,+}$ is found in the inversion-symmetric choice of the unit cell. While sites 1 and 2 belong to the same unit cell, sites 3 and 4, although being in the same honeycomb layer, belong to different unit cells.

The magnon energies $\varepsilon_{n,\boldsymbol{k}}$ and corresponding eigenvectors $|n, \boldsymbol{k}\rangle$ are obtained by a unitary diagonalization of $\mathsf{H}_{\boldsymbol{k}}$. The ferromagnetic order is stable for $|\delta j_\perp| \leqslant \frac{1}{2}\sqrt{(-b+2j_\perp)(-b+2j_\perp+6)}$; note that $b < 0$ for a spin polarization along the z direction. Larger $|\delta j_\perp|$ gives rise to an antiferromagnetic phase.

APPENDIX B: WINDING NUMBER OF A SINGLE HONEYCOMB LAYER

After a Holstein-Primakoff expansion about the ferromagnetic state polarized along the z direction, the bilinear magnon Hamiltonian of a single honeycomb layer reads as $H_2 = \sum_{\boldsymbol{k}} \boldsymbol{\Phi}_{\boldsymbol{k}}^\dagger \cdot \tilde{\mathsf{H}}_{\boldsymbol{k}} \cdot \boldsymbol{\Phi}_{\boldsymbol{k}}$, where $\boldsymbol{\Phi}_{\boldsymbol{k}}^\mathrm{T} = (a_{1,\boldsymbol{k}}, a_{2,\boldsymbol{k}})$ is built from the Fourier-transformed Holstein-Primakoff bosons associated with the two sublattices of the honeycomb. Relying on the well-established analysis of two-level systems [87], the Hamilton kernel

$$\tilde{\mathsf{H}}_{\boldsymbol{k}} = d_{\boldsymbol{k}}^0 \sigma_0 + \boldsymbol{d}_{\boldsymbol{k}} \cdot \boldsymbol{\sigma} \tag{B1}$$

is expanded in terms of Pauli matrices σ_i ($i = 0, 1, 2, 3$). Its eigenvalues read as

$$\varepsilon_{\boldsymbol{k},\pm} = d_{\boldsymbol{k}}^0 \pm |\boldsymbol{d}_{\boldsymbol{k}}|. \tag{B2}$$

As far as topology is concerned, $d_{\boldsymbol{k}}^0 = 3JS + B$ is an irrelevant offset and the crucial information is encoded in the vector $\boldsymbol{d}_{\boldsymbol{k}}$

that determines the winding number

$$w = \frac{1}{4\pi} \int_{\text{BZ}} \frac{\boldsymbol{d_k}}{|\boldsymbol{d_k}|^3} \cdot \left(\frac{\partial \boldsymbol{d_k}}{\partial k_x} \times \frac{\partial \boldsymbol{d_k}}{\partial k_y} \right) dk_x dk_y. \tag{B3}$$

The integration is over the entire Brillouin zone (BZ). The winding number measures how often the unit vector $\boldsymbol{d_k}/|\boldsymbol{d_k}|$ wraps around the unit sphere. Using the explicit expression

$$\boldsymbol{d_k} = \sum_{i=1}^{3} \begin{pmatrix} -JS\cos(\boldsymbol{k} \cdot \boldsymbol{\delta}_i) \\ JS\sin(\boldsymbol{k} \cdot \boldsymbol{\delta}_i) \\ 2DS\sin(\boldsymbol{k} \cdot \boldsymbol{\tau}'_i) \end{pmatrix}, \tag{B4}$$

where the vectors to nearest and second-nearest neighbors are given by

$$\boldsymbol{\delta}_1 = (\sqrt{3}/2, 1/2), \tag{B5a}$$

$$\boldsymbol{\delta}_2 = (-\sqrt{3}/2, 1/2), \tag{B5b}$$

$$\boldsymbol{\delta}_3 = (0, -1), \tag{B5c}$$

and

$$\boldsymbol{\tau}'_1 = (\sqrt{3}, 0), \tag{B6a}$$

$$\boldsymbol{\tau}'_2 = (-\sqrt{3}/2, 3/2), \tag{B6b}$$

$$\boldsymbol{\tau}'_3 = (-\sqrt{3}/2, -3/2), \tag{B6c}$$

respectively, the integral (B3) may be evaluated numerically. Alternatively, one may reexpress the winding number in terms of the sign of the mass term $d_{\boldsymbol{k}}^3$ at the K and K' points of the Brillouin zone as [87,88]

$$w = \tfrac{1}{2}\big[\text{sgn}(d_{\boldsymbol{K'}}^3) - \text{sgn}(d_{\boldsymbol{K}}^3)\big]. \tag{B7}$$

Using $\boldsymbol{K} = (-4\pi/(3\sqrt{3}), 0)$ and $\boldsymbol{K'} = -\boldsymbol{K}$, one obtains

$$d_{\boldsymbol{K}}^3 = -d_{\boldsymbol{K'}}^3 = 3\sqrt{3}DS \tag{B8}$$

and arrives at

$$w = -\text{sgn}(D). \tag{B9}$$

In the stack of honeycomb layers at hand, the sign of DMI alternates between adjacent layers. Hence, the winding number of the lth layer reads as $w^{(l)} = (-1)^l \text{sgn}(D)$.

For a ferromagnetic state pointing along the negative-z direction, one finds $w = \text{sgn}(D)$ because a reversal of the magnetization acts like a reversal of time that flips the chirality of the edge modes. Denoting the ferromagnetic order by $m = \pm 1$, with $m = +1$ ($m = -1$) referring to polarization along the positive- (negative-) z direction, the winding number of each layer reads as $w^{(l)} = (-1)^l \text{sgn}(mD)$.

APPENDIX C: MAGNONIC TOPOLOGICAL CRYSTALLINE INSULATOR PHASES

For $d \neq 0$, $j_\perp \neq 0$ but $\delta j_\perp = 0$, each honeycomb layer is a mirror plane of the entire stack. This gives rise to a nontrivial mirror Chern number [37,89] that stabilizes a surface Dirac cone at the $\overline{L}$ point in the surface Brillouin zone [see surface spectrum in Fig. 10(a)]. Thus, there is nontrivial first-order topology, referred to as "topological crystalline insulator" and labeled $\text{TCI}_{\overline{L}}$.
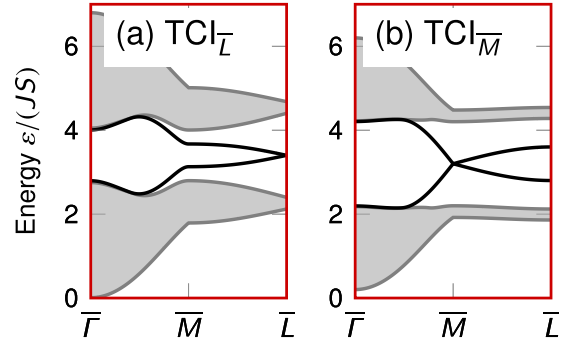

FIG. 10. Magnonic surface Dirac cones in topological crystalline insulating (TCI) phases. (a) For $\delta j_\perp = 0$, the honeycomb layers are mirror planes, stabilizing a surface Dirac cone at the $\overline{L}$ point. Other parameters read as $d = j_\perp = 0.2$ and $b = 0$. (b) For $j_\perp = 0$, a surface Dirac cone at the $\overline{M}$ point is found. Other parameters read as $d = \delta j_\perp = -b = 0.2$. A finite b is necessary to stabilize the ferromagnetic order.

Moreover, for $d \neq 0$, $\delta j_\perp \neq 0$ but $j_\perp = 0$, the coupling along the z direction is alternating in sign, effectively vanishing at $k_z = 0$ and, hence, stabilizing a surface Dirac cone at $\overline{M}$ [denoted as $\text{TCI}_{\overline{M}}$ in Fig. 10(b)]. (Note that $-b \geqslant \sqrt{9 - 4\delta j_\perp^2} - 3$ must hold for a stable ferromagnetic phase at $j_\perp = 0$).

APPENDIX D: SIGN REVERSAL OF $\delta j_\perp$

As explained in Sec. II B, the sign of $\delta j_\perp$ determines whether the SSH-type chains at the surface are topologically trivial or nontrivial. For an even number of layers, this means that the chains' ends either host or do not host end bound states. For an odd number of layers, a dangling spin (hosting the end bound state) is either found at one end or the opposite end. Hence, by reversing the sign of $\delta j_\perp$ the path of hinge magnons has to adapt accordingly.

Figure 11 shows the hinge magnons' probability density for stacks identical to those studied in Fig. 4, with the only difference being the sign of $\delta j_\perp$. One verifies that those hinges at the top and bottom surface that hosted hinge magnons for $\delta j_\perp > 0$ (Fig. 4) do not host hinge magnons for $\delta j_\perp < 0$ (Fig. 11) and vice versa. Note that only the vertical hinges, i.e., those along the stacking direction, must host hinge magnons because of the domain wall pattern being independent of the sign of $\delta j_\perp$. A complete removal of hinge magnons is only possible if there are no domain walls [see Fig. 11(j)] and the stack is built from an even number of layers [see Fig. 11(l)], with the SSH-type chains being topologically trivial.

APPENDIX E: SECOND-ORDER TOPOLOGY FOR INVERSION-SYMMETRIC SAMPLES

A special situation is found for samples that hold spatial symmetries, here, inversion symmetry, as present in Figs. 4(a) and 4(g). A domain wall necessarily is accompanied by another domain wall supporting a counterpropagating mode at the symmetry-related position. The two positions are separated by half of the sample's circumference, the
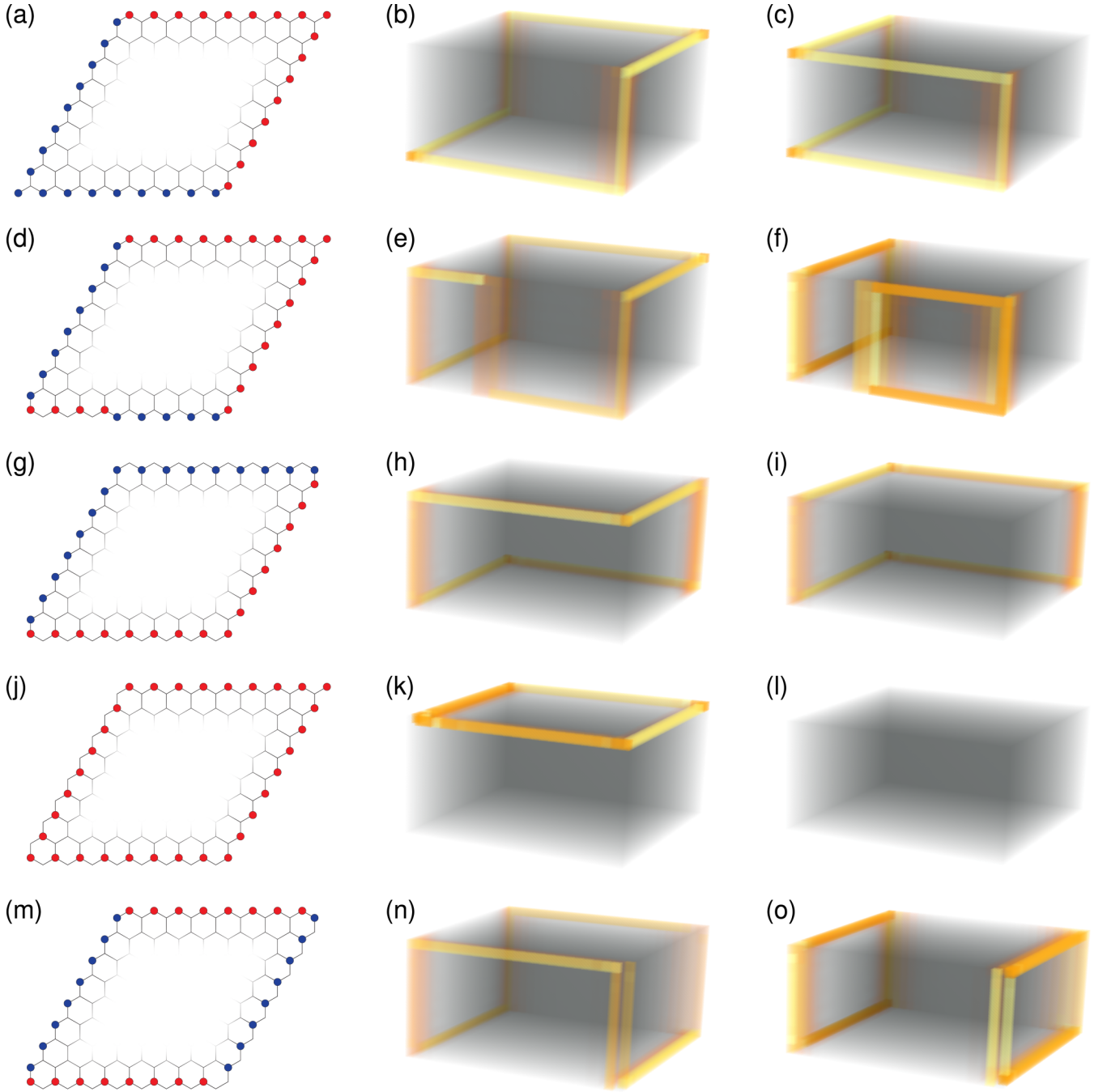
FIG. 11. Same as Fig. 4 but with reversed sign of dimerization pattern: $\delta j_\perp = -0.2$.

largest possible spatial distance, maximally suppressing the hybridization of counterpropagating chiral hinge modes. (We assumed a convex sample cross section). In this spatially symmetric case, a pair of chiral hinge magnons is dictated by a bulk-hinge correspondence [40], a concept recently developed in the field of higher-order topological phases [24–26,90–97]. Here, we demonstrate how to apply these tools to the magnonic case at hand.

For the Fourier kernel $\mathsf{H}_{\boldsymbol{k}}$ of the Hamiltonian in Eq. (A3) we chose a magnetic basis that respects inversion with respect to a hexagon's center of mass. Hence, $\mathsf{H}_{\boldsymbol{k}} = \mathsf{H}_{\boldsymbol{k}+\boldsymbol{G}}$, with $\boldsymbol{G}$ being a reciprocal lattice vector [98]. Inversion symmetry

(or parity symmetry) implies $\mathsf{H}_{\boldsymbol{k}}\mathsf{U} = \mathsf{U}\mathsf{H}_{-\boldsymbol{k}}$, with $\mathsf{U} = \sigma_0 \otimes \sigma_1$. At a time-reversal-invariant momentum (TRIM) $\boldsymbol{\Gamma}_{abc} = (a\boldsymbol{g}_1 + b\boldsymbol{g}_2 + c\boldsymbol{g}_3)/2$, with $a, b, c \in \{0, 1\}$ and the $\boldsymbol{g}_i$'s ($i = 1, 2, 3$) being primitive reciprocal lattice vectors, we thus have $[\mathsf{H}_{\boldsymbol{\Gamma}_{abc}}, \mathsf{U}] = 0$. Consequently, the eigenvectors $|n, \boldsymbol{k} = \boldsymbol{\Gamma}_{abc}\rangle$ of $\mathsf{H}_{\boldsymbol{\Gamma}_{abc}}$ are eigenvectors of U, with parity eigenvalue $p_n(\boldsymbol{\Gamma}_{abc}) = \pm 1$ ($n = 1, \ldots, 4$) [89,98].

As shown in Fig. 3(b), the global band gap appears between the lower and upper pair of bands. Hence, we introduce the number $n_-(\boldsymbol{\Gamma}_{abc})$ [$n_+(\boldsymbol{\Gamma}_{abc})$] of bands below the third band with negative- (positive-) parity eigenvalue at $\boldsymbol{\Gamma}_{abc}$. It enters the quadruple $(\nu_x, \nu_y, \nu_z; \mu_1)$ of symmetry

TABLE I. Energy eigenvalues $\varepsilon_n(\boldsymbol{\Gamma}_{abc})$, parity eigenvalues $p_n(\boldsymbol{\Gamma}_{abc})$ of all magnonic bands ($n = 1, \ldots, 4$) at the eight TRIM $\boldsymbol{\Gamma}_{abc}$. The associated number $n_-(\boldsymbol{\Gamma}_{abc})$ [$n_+(\boldsymbol{\Gamma}_{abc})$] of negative- (positive-) parity eigenvalues of the lowest two bands is given in dependence on $j_\perp$. The small table in the bottom right corner gives the respective symmetry indicators ν_x, ν_y, ν_z, and μ_1, as defined in the text.

TRIM $\boldsymbol{\Gamma}_{abc}$	Name	$\varepsilon_n(\boldsymbol{\Gamma}_{abc})$	$p_n(\boldsymbol{\Gamma}_{abc})$	$n_-(\boldsymbol{\Gamma}_{abc})$ [$n_+(\boldsymbol{\Gamma}_{abc})$]		
				$j_\perp < \frac{1}{2}$	$\frac{1}{2} < j_\perp < \frac{3}{2}$	$\frac{3}{2} < j_\perp$
$\boldsymbol{\Gamma}_{000}$	Γ	$-b$	$+1$			
		$-b + 4j_\perp$	$+1$			
		$-b + 6$	-1	0[2]	0[2]	1[1]
		$-b + 6 + 4j_\perp$	-1			
$\boldsymbol{\Gamma}_{010}, \boldsymbol{\Gamma}_{100}, \boldsymbol{\Gamma}_{110}$	M	$-b + 2$	-1			
		$-b + 2 + 4j_\perp$	-1			
		$-b + 4$	$+1$	2[0]	1[1]	1[1]
		$-b + 4 + 4j_\perp$	$+1$			
$\boldsymbol{\Gamma}_{001}$	A	$-b + 3 + 2j_\perp - \sqrt{9 + 4\delta j_\perp^2}$	$+1$			
		$-b + 3 + 2j_\perp - \sqrt{9 + 4\delta j_\perp^2}$	-1			
		$-b + 3 + 2j_\perp + \sqrt{9 + 4\delta j_\perp^2}$	$+1$	1[1]	1[1]	1[1]
		$-b + 3 + 2j_\perp + \sqrt{9 + 4\delta j_\perp^2}$	-1			
$\boldsymbol{\Gamma}_{011}, \boldsymbol{\Gamma}_{101}, \boldsymbol{\Gamma}_{111}$	L	$-b + 3 + 2j_\perp - \sqrt{1 + 4\delta j_\perp^2}$	$+1$			
		$-b + 3 + 2j_\perp - \sqrt{1 + 4\delta j_\perp^2}$	-1			
		$-b + 3 + 2j_\perp + \sqrt{1 + 4\delta j_\perp^2}$	$+1$	1[1]	1[1]	1[1]
		$-b + 3 + 2j_\perp + \sqrt{1 + 4\delta j_\perp^2}$	-1			
		Symmetry indicator		$j_\perp < \frac{1}{2}$	$\frac{1}{2} < j_\perp < \frac{3}{2}$	$\frac{3}{2} < j_\perp$
			ν_x	0	0	0
			ν_y	0	0	0
			ν_z	0	0	0
			μ_1	2	3	0

indicators [40,99–103], which is used to characterize second-order topology. The weak indices read as [40]

$$\nu_x = \sum_{b=0,1} \sum_{c=0,1} n_-(\boldsymbol{\Gamma}_{1bc}) \bmod 2, \qquad \text{(E1a)}$$

$$\nu_y = \sum_{a=0,1} \sum_{c=0,1} n_-(\boldsymbol{\Gamma}_{a1c}) \bmod 2, \qquad \text{(E1b)}$$

$$\nu_z = \sum_{a=0,1} \sum_{b=0,1} n_-(\boldsymbol{\Gamma}_{ab1}) \bmod 2, \qquad \text{(E1c)}$$

and the strong index [40]

$$\mu_1 = \sum_{a=0,1} \sum_{b=0,1} \sum_{c=0,1} \frac{n_+(\boldsymbol{\Gamma}_{abc}) - n_-(\boldsymbol{\Gamma}_{abc})}{2}$$

$$= -\sum_{a=0,1} \sum_{b=0,1} \sum_{c=0,1} n_-(\boldsymbol{\Gamma}_{abc}) \bmod 4. \qquad \text{(E2)}$$

Nonzero ν_α's imply weak Chern insulators stacked in $\alpha = x, y, z$ direction. In contrast, the $\mathbb{Z}_4$ indicator μ_1 is innately 3D. If μ_1 is odd, the Chern numbers in the $k_z = 0$ and π planes are opposite, enforcing a band crossing somewhere in-between; this implies a first-order topological Weyl semimetal phase [104,105]. In contrast, no crossing is enforced for even μ_1, admitting of either trivial ($\mu_1 = 0$) or nontrivial ($\mu_1 = 2$) band gaps [103].

The parity eigenvalues of the four magnon bands are listed in Table I. Since the basis is chosen with respect to a center of inversion that respects the symmetries of the hexagonal lattice,

the three M points ($\boldsymbol{\Gamma}_{010}$, $\boldsymbol{\Gamma}_{100}$, $\boldsymbol{\Gamma}_{110}$) exhibit the same parity eigenvalues; so do the three L points ($\boldsymbol{\Gamma}_{011}$, $\boldsymbol{\Gamma}_{101}$, $\boldsymbol{\Gamma}_{111}$). Note that $j_\perp$ determines the energetic order of the bands. Hence, the numbers of bands with negative- and positive-parity eigenvalues below the third band also depend on $j_\perp$. So do the
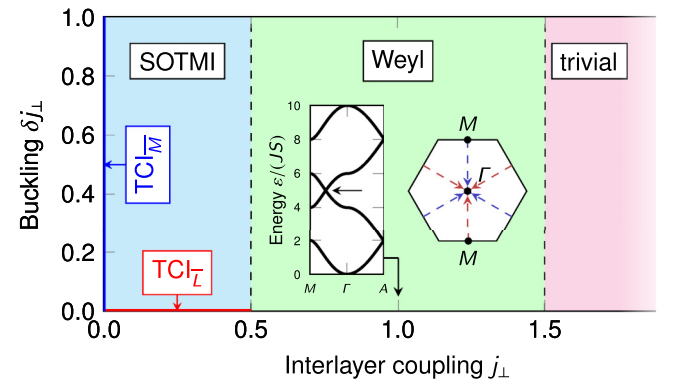

FIG. 12. Topological magnon phase diagram of a stack of ferromagnetic honeycomb layers. For $j_\perp < \frac{1}{2}$, a second-order topological magnon insulator (SOTMI) is found, bounded by two topological crystalline insulating (TCI) phases, with surface Dirac cones either at $\overline{L}$ (TCI$_{\overline{L}}$) or $\overline{M}$ (TCI$_{\overline{M}}$); see Appendix C. At $j_\perp = \frac{1}{2}$, pairs of Weyl points of opposite topological charge split from the $\overline{M}$ points and, as $j_\perp$ increases up to $\frac{3}{2}$, move to the Γ point, where they annihilate (see insets), giving rise to a trivial insulator phase for $\frac{3}{2} < j_\perp$.
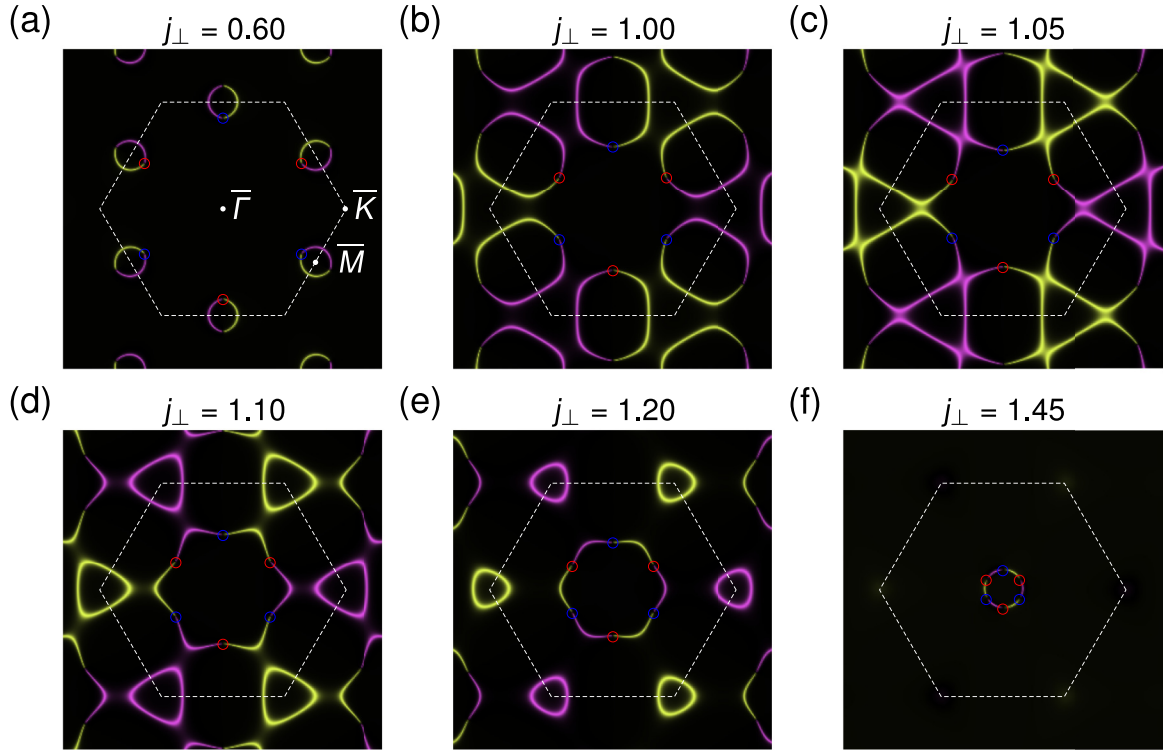
FIG. 13. Evolution of magnon arcs at the surface of the magnonic Weyl semimetallic phase. A stack of finite height with open boundary conditions in the stacking direction (z direction) but periodic boundary conditions in the honeycomb planes (x and y directions) exhibits six projections of Weyl points within the surface Brillouin zone (see circles). The circles' color indicates the opposite topological charge of the Weyl points (red vs blue). The color plot depicts the spectral function at the energy of the Weyl points, with yellow (pink) features being located at the bottom (top) surface of the stack. For $j_\perp > 0.5$, a pair of Weyl points splits from the $\overline{M}$ points (a). Oppositely charged Weyl points move in opposite directions towards the $\overline{\Gamma}$ point as $j_\perp$ increases (b)–(f). Eventually, the Weyl points annihilate at the $\overline{\Gamma}$ point for $j_\perp = 1.5$. The magnon arcs always connect Weyl point projections of opposite topological charge. Other parameters read as $d = \delta j_\perp = 0.2$ and $b = 0$.

symmetry indicators, given in the small table in the bottom right corner.

Overall, we obtain the topological phase diagram in Fig. 12. The weak indices ν_x, ν_y, and ν_z are always trivial (cf. small bottom right table in Table I), signaling the absence of weak topology. In contrast, for the physically most relevant scenario of weakly coupled layers $j_\perp < \frac{1}{2}$, a strong nontrivial indicator of second-order topology is found ($\mu_1 = 2$), dictating the existence of chiral hinge magnons. However, we reiterate that inversion symmetry is not necessary to obtain hinge magnons. They are robust against both inversion-asymmetric sample shapes (cf. Fig. 4) as well as magnetic interactions (see Appendix F).

Stronger interlayer coupling, $\frac{1}{2} < j_\perp < \frac{3}{2}$, causes a semimetallic phase with Weyl magnons [106–109] ($\mu_1 = 3$). At $j_\perp = \frac{1}{2}$, pairs of oppositely charged Weyl points split from the M points. As $j_\perp$ increases, they move along $M \to \Gamma$ until they meet at Γ, where they annihilate (see insets in Fig. 12). At the surfaces of the stack Weyl point projections of opposite charge are connected by magnon arcs, as depicted in Fig. 13. After the Weyl points have annihilated, a topologically trivial insulating system is found for $\frac{3}{2} < j_\perp$ ($\mu_1 = 0$), which does not exhibit chiral hinge magnons.

The topological invariants are independent of d and $\delta j_\perp$; still, these parameters are necessary to ensure that there is a bulk and surface gap, respectively, in the SOTMI phase.

For $d = 0$, there is no bulk gap to begin with, rendering a discussion of hinge modes moot. Finite $\delta j_\perp$ is necessary to break mirror symmetry (see Appendix C).

APPENDIX F: EFFECTS OF BROKEN INVERSION SYMMETRY

The symmetry indicator μ_1 in Eq. (E2) relies on inversion symmetry, a crystalline symmetry that is easily broken in any real material, e.g., by finite-density disorder or inversion-asymmetric sample shapes. The robustness of chiral hinge states against disorder is studied in Sec. II D and Appendix G 2. Here, we provide further evidence that inversion symmetry is not a prerequisite for chiral hinge magnons by showing that inversion-symmetry-breaking perturbations do not jeopardize their stability. Three perturbations are considered:

$$H_{\text{pert}} = \sum_l \sum_i B_i^z S_i^{(l),z}$$
$$- K_A \sum_l \sum_{i \in A} \left(S_i^{(l),z}\right)^2 - K_B \sum_l \sum_{i \in B} \left(S_i^{(l),z}\right)^2$$
$$+ \frac{\delta D}{2} \sum_l \sum_{\langle\langle ij \rangle\rangle} \nu_{ij} \hat{z} \cdot \mathbf{S}_i^{(l)} \times \mathbf{S}_j^{(l)}, \tag{F1}$$
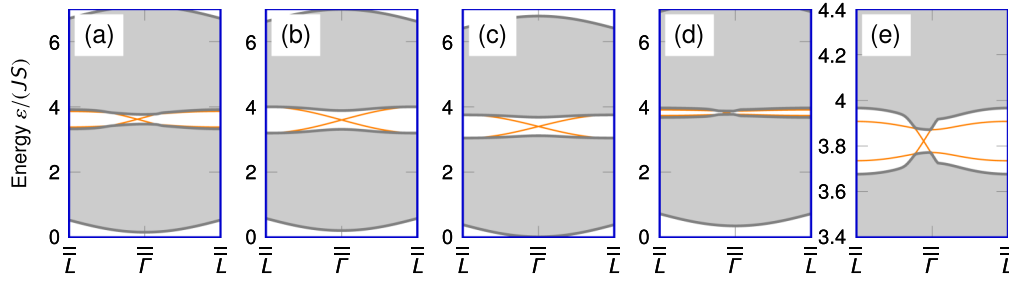
FIG. 14. Magnon spectrum of an infinite stack of honeycomb layers with nontrivial second-order topology in the presence of perturbations. The pillar has an all-zigzag terminated parallelogram cross section. The gray continua indicate projected bulk and surface states. The orange lines indicate hinge states. For all cases, these hinge states are chiral. (a) In the presence of a magnetic-field gradient $\nabla_x B^z/J = 0.008/a$ (a lattice spacing) inversion symmetry is broken. (b) A sublattice-asymmetric easy-axis anisotropy ($K_A/J = 0.2$ and $K_B/J = 0$) also breaks inversion symmetry. (c) For $\delta D/J = 0.1$, adjacent layers have DMI that is not exactly opposite. (d) All perturbations combined, with (e) showing a blowup of the spectral gap. Other parameters read as $d = j_\perp = \delta j_\perp = 0.2$ and $b = 0$.

(1) a magnetic field gradient ∇B^z (the local magnetic fields B_i^z are chosen accordingly), (2) sublattice-dependent easy-axis anisotropies $K_A > 0$ and $K_B > 0$, and (3) layer-asymmetric modulus of DMI by adding positive δD to all second-nearest-neighbor bonds. The first two perturbations break inversion symmetry. The latter does not but it removes the constraint of exactly opposite DMI.

Figure 14 shows pillar band structures in the presence of the above perturbations. The pillar's cross section is a parallelogram with all-zigzag termination, similar to that shown in Fig. 11(a). For a magnetic field gradient along the x direction, the two hinge states experience different rigid energy shifts. Hence, in the spectrum the crossing of the hinge modes is no longer found at the $\overline{\overline{\Gamma}}$ point but at nonzero k_z [see Fig. 14(a)]. Nonzero K_A and K_B effectively create onsite potentials for magnons. For $K_A \neq K_B$, inversion symmetry is broken. Nonetheless, as long as these potentials are not strong enough to close the gap, chiral hinge magnons remain robust [see Fig. 14(b)]. Finite δD models the situation that the alternating layers do not have exactly opposite DMI. Although this does not break inversion symmetry, we point out that the chiral hinge states are robust [see Fig. 14(c)] even in this more general model. Finally, Fig. 14(d) depicts the pillar band structure in the simultaneous presence of all these perturbations. Although the gap is considerably decreased, Fig. 14(e) proves that there are still chiral hinge magnons.

We conclude that spin Hamiltonian (1) does not have to be "fine tuned" to yield nontrivial second-order topology for magnons. Quite in contrast, even strong perturbations with energy scales similar to that of D and $\delta j_\perp$ do not destroy chiral hinge magnons. The same robustness is expected against perturbations that break the U(1) spin rotation symmetry about the z direction, e.g., dipolar interactions.

APPENDIX G: ATOMISTIC SPIN DYNAMICS SIMULATIONS

1. General comments

Due to the semiclassical nature of the harmonic magnon theory, the nontrivial topology of spin waves can be captured by classical spin dynamics. It is based on the equation of

motion $\hbar \dot{\mathbf{S}}_i(t) = -\mathbf{S}_i(t) \times \mathbf{B}_i(t)$, describing the precession of each spin vector $\mathbf{S}_i$ in the effective magnetic field $\mathbf{B}_i$ due to its neighbors. Here, t denotes time. For simplicity, Gilbert damping is neglected and temperature is set to zero.

Starting from the fully polarized ferromagnetic ground state (along the z direction), we apply a dynamic magnetic field $\mathbf{b}_r = b_0 \sin(t\varepsilon_{ex}/\hbar)\hat{\mathbf{x}}$ to a single spin (index r); $\hat{\mathbf{x}}$ is a unit vector along the x direction. It causes a coherent excitation of magnons at energy ε_{ex}, provided they have finite probability density at site r. A small amplitude $b_0 \ll 1$ is chosen to avoid nonlinear dynamics (which correspond to magnon-magnon interactions). To trace the excitation, we measure the discrete amplitude $A_i(t) = \sqrt{[S_i^x(t)]^2 + [S_i^y(t)]^2}$ of each spin upon numerical integration of the equation of motion. For plotting, we convert $A_i(t)$ into a continuous density $A(t, \mathbf{r})$, with $\mathbf{r}$ denoting the position in the finite sample.

We consider a finite-sized sample with 30 or 31 layers of 40×40 honeycomb unit cells with "compensated" boundaries (see Appendix H for explanation). The cross section of the pillar is a parallelogram with all-zigzag termination, hosting chiral hinge magnons at the two opposite obtuse corners [cf. Figs. 3(e), 4(b), and 4(c)]. We set $\varepsilon_{ex}/(JS) = 3.4$, which is right in the middle of the global band gap [cf. Fig. 3(d)].

2. Simulations with disorder

The excited spin is situated at an obtuse hinge but the bulk is disordered. We add random magnetic fields b_i^z, drawn from a uniform distribution $[-\frac{\beta}{2}, \frac{\beta}{2}]$, to *all* spins. For small disorder strengths, such that their standard deviation $\sigma_b = \beta/(2\sqrt{3})$ is smaller than the surface gap $\Delta \approx 0.54$ [cf. Fig. 3(d)], the chiral hinge magnons survive; see Figs. 15(a)–15(c). However, once σ_b approaches Δ, disorder slows down the hinge magnons and eventually causes localization of the formerly propagating hinge magnons; see Figs. 15(d) and 15(e). For movies, see Supplemental Material, videos 5–9 [41]: SuppMov5.mov, SuppMov6.mov, SuppMov7.mov, SuppMov8.mov, SuppMov9.mov. The respective ratios $R = \sigma_b/\Delta$ between disorder strength and band gap are $R = 0.21$, 0.43, 0.64, 0.86, and 1.07.

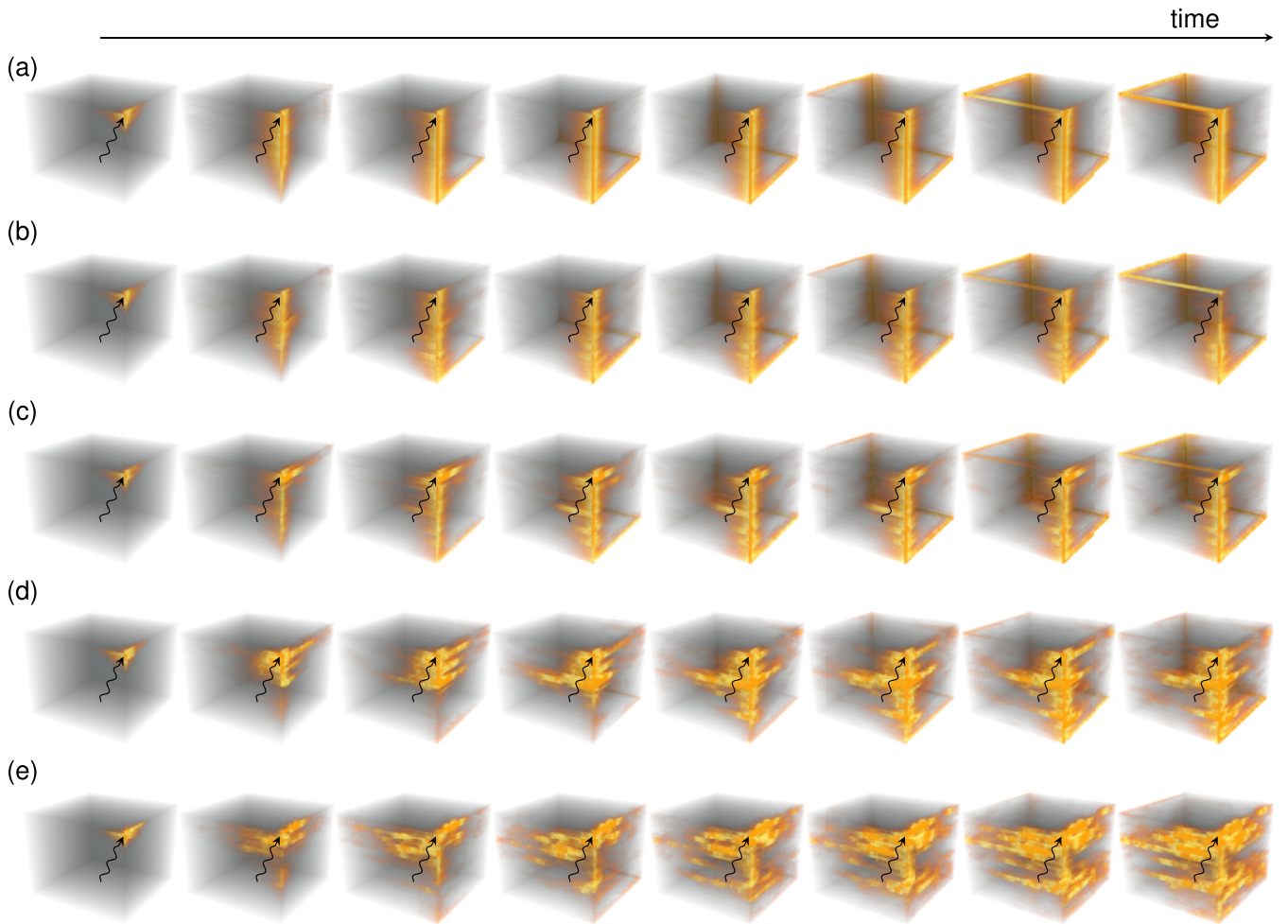time

FIG. 15. Snapshots of Supplemental Material, videos 5–9 [41]: (a) `SuppMov5.mov`, (b) `SuppMov6.mov`, (c) `SuppMov7.mov`, (d) `SuppMov8.mov`, and (e) `SuppMov9.mov`. From top to bottom, the rows show simulations with increasing disorder, (a) $R = 0.21$, (b) $R = 0.43$, (c) $R = 0.64$, (d) $R = 0.86$, and (e) $R = 1.07$, where $R = \sigma_b/\Delta$ gives the ratio of disorder strength σ_b and the surface band gap Δ. Upon exciting a spin at an obtuse hinge, a chiral magnon is launched, whose propagation is severely hindered once $R \gtrsim 1$.

APPENDIX H: ANALYSIS OF "UNCOMPENSATED" BOUNDARIES

Throughout this work, we discussed the ideal case of "compensated" boundaries. To explain this term, we first discuss "uncompensated" boundaries. Boundary spins have a lower coordination number than bulk spins. Hence, the effective field acting on a surface spin is reduced, lowering its excitations in energy. (Colloquially speaking, surface spins are "more floppy" than bulk spins). This causes a downward shift of the surface states, as shown in Fig. 16(a), if we leave the surface "uncompensated." As a consequence, the surface band gap is decreased [Fig. 16(b)] and the hinges also host trivial states that may hybridize with the chiral states [Fig. 16(c)], whose existence is still dictated by bulk topology.

There are several additional effects of this downward shift: First, the small surface band gap causes a spread of the hinge states, i.e., their probability density is less sharply localized at the hinges. Second, there are critical values for d and $\delta j_{\perp}$, below which a global band gap is absent. Figure 17 depicts the global gap, i.e., the overlap of bulk and surface gap, in the SOTMI phase for selected values of d and "uncompensated"

boundaries. For too small a d, the surface gap and bulk gap do not overlap, because the surface gap at $\overline{M}$ is below bulk states
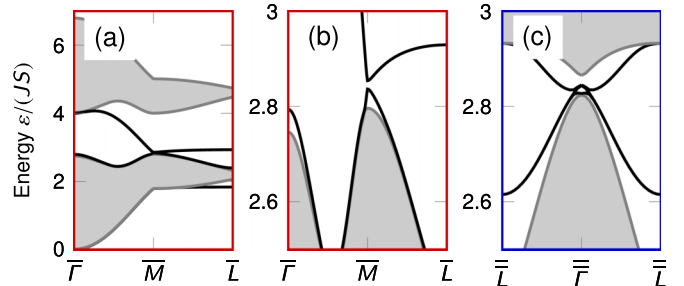

FIG. 16. Magnonic spectra for "uncompensated" boundaries. (a) 2D surface magnon spectrum, with gray continuum indicating projected bulk states and sharp black lines surface states. Compared to Fig. 3(c), the surface states are shifted downwards in energy with respect to the bulk states. (b) Zoom into the surface band gap. (c) Gapless 1D spectrum with chiral hinge magnons (black lines). The chiral modes hybridize with a trivial surface state that does not cross the band gap.
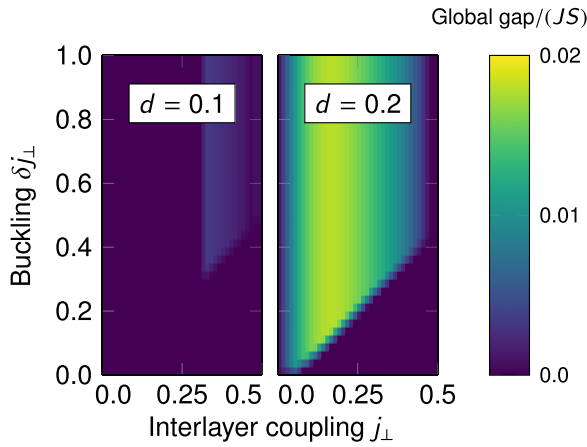
FIG. 17. Global band gap, defined as the overlap of the bulk and surface band gap, for selected values of d in dependence on $j_\perp$ and $\delta j_\perp$. "Uncompensated boundaries" are considered. When the surface and bulk band gaps do not overlap, the global gap vanishes (dark blue color).
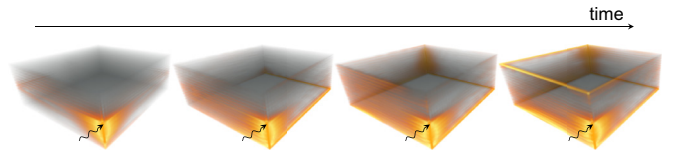

FIG. 18. Snapshots of Supplemental Material, video 10: `SuppMov10.mov`. A stack of 31 layers with "uncompensated" boundaries of 80×80 honeycomb unit cells is simulated.

at the $\overline{K}$ points (surface projections of the K and K' points of the 3D BZ); hence, there is no global gap. Moreover, for too small a $\delta j_\perp$, the surface gaps at $\overline{M}$ and $\overline{L}$ do not overlap, also yielding zero global gap. We find that $d \gtrsim 0.16$ and $\delta j_\perp \gtrsim j_\perp$ ensure a finite global gap for "uncompensated boundaries."

We also considered "uncompensated" boundaries in our spin dynamics simulations. A sample size of 31 layers of

80×80 honeycomb unit cells is simulated, with $\varepsilon_{\mathrm{ex}}/(JS) = 2.85$ [well within the surface gap; cf. Fig. 16(c)]. Again, the excitation travels along the hinges but also spreads considerably along the neighboring surfaces due to the less sharply localized wave function of the hinge magnon (see Fig. 18). For a movie, see Supplemental Material, video 10 [41]: `SuppMov10.mov`.

To engineer the surfaces the finite-size system could be immersed in (or its surfaces proximitized to) another magnet with an overlapping but topologically trivial band gap. Then, the coordination number of boundary spins equals that of the bulk spins and boundary states are shifted upwards again. Throughout this work, we simulated such "compensated" boundaries by boundary-located magnetic fields that exactly compensate for missing neighbors. Overall, the difference between "compensated" and "uncompensated" boundaries offers another degree of freedom for the design of hinge magnons, which may be exploited in future magnonic architectures.

[1] K. von Klitzing, The quantized Hall effect, Rev. Mod. Phys. **58**, 519 (1986).

[2] O. A. Pankratov, Supersymmetric inhomogeneous semiconductor structures and the nature of a parity anomaly in (2+1) electrodynamics, Phys. Lett. A **121**, 360 (1987).

[3] F. D. M. Haldane, Model for a Quantum Hall Effect without Landau Levels: Condensed-Matter Realization of the "Parity Anomaly", Phys. Rev. Lett. **61**, 2015 (1988).

[4] L. Zhang, J. Ren, J.-S. Wang, and B. Li, Topological magnon insulator in insulating ferromagnet, Phys. Rev. B **87**, 144101 (2013).

[5] R. Shindou, R. Matsumoto, S. Murakami, and J.-I. Ohe, Topological chiral magnonic edge mode in a magnonic crystal, Phys. Rev. B **87**, 174427 (2013).

[6] A. Mook, J. Henk, and I. Mertig, Edge states in topological magnon insulators, Phys. Rev. B **90**, 024412 (2014).

[7] A. Roldán-Molina, A. S. Nunez, and J. Fernández-Rossier, Topological spin waves in the atomic-scale magnetic skyrmion crystal, New J. Phys. **18**, 045015 (2016).

[8] K. Nakata, S. K. Kim, J. Klinovaja, and D. Loss, Magnonic topological insulators in antiferromagnets, Phys. Rev. B **96**, 224414 (2017).

[9] S. A. Díaz, J. Klinovaja, and D. Loss, Topological Magnons and Edge States in Antiferromagnetic Skyrmion Crystals, Phys. Rev. Lett. **122**, 187203 (2019).

[10] F. Meier and D. Loss, Magnetization Transport and Quantized Spin Conductance, Phys. Rev. Lett. **90**, 167204 (2003).

[11] H. Katsura, N. Nagaosa, and P. A. Lee, Theory of the Thermal Hall Effect in Quantum Magnets, Phys. Rev. Lett. **104**, 066403 (2010).

[12] R. Matsumoto and S. Murakami, Theoretical Prediction of a Rotating Magnon Wave Packet in Ferromagnets, Phys. Rev. Lett. **106**, 197202 (2011).

[13] K. A. van Hoogdalem, Y. Tserkovnyak, and D. Loss, Magnetic texture-induced thermal Hall effects, Phys. Rev. B **87**, 024402 (2013).

[14] A. Mook, J. Henk, and I. Mertig, Magnon Hall effect and topology in kagome lattices: A theoretical investigation, Phys. Rev. B **89**, 134409 (2014).

[15] K. Nakata, J. Klinovaja, and D. Loss, Magnonic quantum Hall effect and Wiedemann-Franz law, Phys. Rev. B **95**, 125429 (2017).

[16] A. Mook, B. Göbel, J. Henk, and I. Mertig, Taking an electron-magnon duality shortcut from electron to magnon transport, Phys. Rev. B **97**, 140401(R) (2018).

[17] S. K. Kim, K. Nakata, D. Loss, and Y. Tserkovnyak, Tunable Magnonic Thermal Hall Effect in Skyrmion Crystal Phases of Ferrimagnets, Phys. Rev. Lett. **122**, 057204 (2019).

[18] A. V. Chumak, V. I. Vasyuchka, A. A. Serga, and B. Hillebrands, Magnon spintronics, Nat. Phys. **11**, 453 (2015).

[19] X. S. Wang, H. W. Zhang, and X. R. Wang, Topological Magnonics: A Paradigm for Spin-Wave Manipulation and Device Design, Phys. Rev. Appl. **9**, 024029 (2018).

[20] K. Yamamoto, G. C. Thiang, P. Pirro, K.-W. Kim, K. Everschor-Sitte, and E. Saitoh, Topological Characterization of Classical Waves: The Topological Origin of Magnetostatic Surface Spin Waves, Phys. Rev. Lett. **122**, 217201 (2019).

[21] S. A. Díaz, T. Hirosawa, J. Klinovaja, and D. Loss, Chiral magnonic edge states in ferromagnetic skyrmion crystals controlled by magnetic fields, Phys. Rev. Res. **2**, 013231 (2020).

[22] E. Aguilera, R. Jaeschke-Ubiergo, N. Vidal-Silva, L. E. F. F. Torres, and A. S. Nunez, Topological magnonics in the two-dimensional van der Waals magnet CrI_3, Phys. Rev. B **102**, 024409 (2020).

[23] A. W. Topol, D. C. L. Tulipe, L. Shi, D. J. Frank, K. Bernstein, S. E. Steen, A. Kumar, G. U. Singco, A. M. Young, K. W. Guarini *et al.*, Three-dimensional integrated circuits, IBM J. Res. Dev. **50**, 491 (2006).

[24] W. A. Benalcazar, B. A. Bernevig, and T. L. Hughes, Quantized electric multipole insulators, Science **357**, 61 (2017).

[25] F. Schindler, A. M. Cook, M. G. Vergniory, Z. Wang, S. S. P. Parkin, B. A. Bernevig, and T. Neupert, Higher-order topological insulators, Sci. Adv. **4**, eaat0346 (2018).

[26] F. Schindler, Z. Wang, M. G. Vergniory, A. M. Cook, A. Murani, S. Sengupta, A. Y. Kasumov, R. Deblock, S. Jeon, I. Drozdov *et al.*, Higher-order topology in bismuth, Nat. Phys. **14**, 918 (2018).

[27] Z. Li, Y. Cao, P. Yan, and X. Wang, Higher-order topological solitonic insulators, npj Comput. Mater. **5**, 107 (2019).

[28] A. Sil and A. K. Ghosh, First and second order topological phases on ferromagnetic breathing kagome lattice, J. Phys.: Condens. Matter **32**, 205601 (2020).

[29] T. Hirosawa, S. A. Díaz, J. Klinovaja, and D. Loss, Magnonic Quadrupole Topological Insulator in Antiskyrmion Crystals, Phys. Rev. Lett. **125**, 207204 (2020).

[30] K. Wagner, A. Kákay, K. Schultheiss, A. Henschke, T. Sebastian, and H. Schultheiss, Magnetic domain walls as reconfigurable spin-wave nanochannels, Nat. Nanotechnol. **11**, 432 (2016).

[31] A. Haldar, D. Kumar, and A. O. Adeyeye, A reconfigurable waveguide for energy-efficient transmission and local manipulation of information in a nanomagnetic device, Nat. Nanotechnol. **11**, 437 (2016).

[32] D. Grundler, Nanomagnonics around the corner, Nat. Nanotechnol. **11**, 407 (2016).

[33] S. A. Owerre, A first theoretical realization of honeycomb topological magnon insulator, J. Phys.: Condens. Matter **28**, 386001 (2016).

[34] I. Dzyaloshinsky, A thermodynamic theory of "weak" ferromagnetism of antiferromagnetics, J. Phys. Chem. Sol. **4**, 241 (1958).

[35] T. Moriya, Anisotropic Superexchange Interaction and Weak Ferromagnetism, Phys. Rev. **120**, 91 (1960).

[36] W. Zhang, P. K. J. Wong, R. Zhu, and A. T. S. Wee, Van der Waals magnets: Wonder building blocks for two-dimensional spintronics? InfoMat **1**, 479 (2019).

[37] I. C. Fulga, N. Avraham, H. Beidenkopf, and A. Stern, Coupled-layer description of topological crystalline insulators, Phys. Rev. B **94**, 125405 (2016).

[38] A. H. Castro Neto, F. Guinea, N. M. R. Peres, K. S. Novoselov, and A. K. Geim, The electronic properties of graphene, Rev. Mod. Phys. **81**, 109 (2009).

[39] W. P. Su, J. R. Schrieffer, and A. J. Heeger, Solitons in Polyacetylene, Phys. Rev. Lett. **42**, 1698 (1979).

[40] R. Takahashi, Y. Tanaka, and S. Murakami, Bulk-edge and bulk-hinge correspondence in inversion-symmetric insulators, Phys. Rev. Res. **2**, 013300 (2020).

[41] See Supplemental Material at http://link.aps.org/supplemental/10.1103/PhysRevB.104.024406 for 10 movies of spin dynamics simulations.

[42] A. K. Geim and I. V. Grigorieva, Van der Waals heterostructures, Nature (London) **499**, 419 (2013).

[43] M. Gibertini, M. Koperski, A. F. Morpurgo, and K. S. Novoselov, Magnetic 2D materials and heterostructures, Nat. Nanotechnol. **14**, 408 (2019).

[44] B. Huang, G. Clark, E. Navarro-Moratalla, D. R. Klein, R. Cheng, K. L. Seyler, D. Zhong, E. Schmidgall, M. A. McGuire, D. H. Cobden *et al.*, Layer-dependent ferromagnetism in a van der Waals crystal down to the monolayer limit, Nature (London) **546**, 270 (2017).

[45] L. Thiel, Z. Wang, M. A. Tschudin, D. Rohner, I. Gutiérrez-Lezama, N. Ubrig, M. Gibertini, E. Giannini, A. F. Morpurgo, and P. Maletinsky, Probing magnetism in 2D materials at the nanoscale with single-spin microscopy, Science **364**, 973 (2019).

[46] W. Chen, Z. Sun, Z. Wang, L. Gu, X. Xu, S. Wu, and C. Gao, Direct observation of van der Waals stacking–dependent interlayer magnetism, Science **366**, 983 (2019).

[47] B. Huang, G. Clark, D. R. Klein, D. MacNeill, E. Navarro-Moratalla, K. L. Seyler, N. Wilson, M. A. McGuire, D. H. Cobden, D. Xiao *et al.*, Electrical control of 2D magnetism in bilayer CrI3, Nat. Nanotechnol. **13**, 544 (2018).

[48] T. P. Lyons, D. Gillard, A. Molina-Sánchez, A. Misra, F. Withers, P. S. Keatley, A. Kozikov, T. Taniguchi, K. Watanabe, K. S. Novoselov *et al.*, Interplay between spin proximity effect and charge-dependent exciton dynamics in $MoSe_2$/$CrBr_3$ van der Waals heterostructures, Nat. Commun. **11**, 6021 (2020).

[49] L. Chen, J.-H. Chung, B. Gao, T. Chen, M. B. Stone, A. I. Kolesnikov, Q. Huang, and P. Dai, Topological Spin Excitations in Honeycomb Ferromagnet CrI_3, Phys. Rev. X **8**, 041028 (2018).

[50] L. Chen, J.-H. Chung, T. Chen, C. Duan, A. Schneidewind, I. Radelytskyi, D. J. Voneshen, R. A. Ewings, M. B. Stone, A. I. Kolesnikov *et al.*, Magnetic anisotropy in ferromagnetic CrI_3, Phys. Rev. B **101**, 134418 (2020).

[51] A. T. Costa, D. L. R. Santos, N. M. R. Peres, and J. Fernández-Rossier, Topological magnons in CrI_3 monolayers: an itinerant fermion description, 2D Mater. **7**, 045031 (2020).

[52] C. Xu, J. Feng, H. Xiang, and L. Bellaiche, Interplay between Kitaev interaction and single ion anisotropy in ferromagnetic CrI_3 and $CrGeTe_3$ monolayers, npj Comput. Mater. **4**, 57 (2018).

[53] C. Xu, J. Feng, S. Prokhorenko, Y. Nahas, H. Xiang, and L. Bellaiche, Topological spin texture in Janus monolayers of the chromium trihalides $Cr(I, X)_3$, Phys. Rev. B **101**, 060404(R) (2020).

[54] I. Lee, F. G. Utermohlen, D. Weber, K. Hwang, C. Zhang, J. van Tol, J. E. Goldberger, N. Trivedi, and P. C. Hammel, Fundamental Spin Interactions Underlying the Magnetic Anisotropy in the Kitaev Ferromagnet CrI_3, Phys. Rev. Lett. **124**, 017201 (2020).

[55] M. Pizzochero, R. Yadav, and O. V. Yazyev, Magnetic exchange interactions in monolayer CrI$_3$ from many-body wavefunction calculations, 2D Mater. **7**, 035005 (2020).

[56] R. Jaeschke-Ubiergo, E. S. Morell, and A. S. Nunez, Theory of magnetism in the van der Waals magnet CrI$_3$, Phys. Rev. B **103**, 174410 (2021).

[57] W.-B. Zhang, Q. Qu, P. Zhu, and C.-H. Lam, Robust intrinsic ferromagnetism and half semiconductivity in stable two-dimensional single-layer chromium trihalides, J. Mater. Chem. C **3**, 12457 (2015).

[58] E. J. Samuelsen, R. Silberglitt, G. Shirane, and J. P. Remeika, Spin waves in ferromagnetic CrBr$_3$ studied by inelastic neutron scattering, Phys. Rev. B **3**, 157 (1971).

[59] D. Soriano, M. I. Katsnelson, and J. Fernández-Rossier, Magnetic Two-Dimensional Chromium Trihalides: A Theoretical Perspective, Nano Letters **20**, 6225 (2020).

[60] S. Hofer, T. Datta, S. Tewari, and D. Mazumdar, Topological properties of multilayer magnon insulators, arXiv:2008.05487.

[61] R. Hidalgo-Sacoto, R. I. Gonzalez, E. E. Vogel, S. Allende, J. D. Mella, C. Cardenas, R. E. Troncoso, and F. Munoz, Magnon valley Hall effect in CrI$_3$-based van der Waals heterostructures, Phys. Rev. B **101**, 205425 (2020).

[62] J. Liang, W. Wang, H. Du, A. Hallal, K. Garcia, M. Chshiev, A. Fert, and H. Yang, Very large Dzyaloshinskii-Moriya interaction in two-dimensional Janus manganese dichalcogenides and its application to realize skyrmion states, Phys. Rev. B **101**, 184401 (2020).

[63] J. Yuan, Y. Yang, Y. Cai, Y. Wu, Y. Chen, X. Yan, and L. Shen, Intrinsic skyrmions in monolayer Janus magnets, Phys. Rev. B **101**, 094420 (2020).

[64] A. Mook, K. Plekhanov, J. Klinovaja, and D. Loss, Interaction-Stabilized Topological Magnon Insulator in Ferromagnets, Phys. Rev. X **11**, 021061 (2021).

[65] M. E. Zhitomirsky and A. L. Chernyshev, Colloquium: Spontaneous magnon decays, Rev. Mod. Phys. **85**, 219 (2013).

[66] A. L. Chernyshev and P. A. Maksimov, Damped Topological Magnons in the Kagome-Lattice Ferromagnets, Phys. Rev. Lett. **117**, 187203 (2016).

[67] A. V. Chumak, Magnon spintronics, in *Spintronics Handbook: Spin Transport and Magnetism*, 2nd ed., 247 (CRC Press, Boca Raon, FL, 2019).

[68] A. Brataas, Y. Tserkovnyak, and G. E. W. Bauer, Scattering Theory of Gilbert Damping, Phys. Rev. Lett. **101**, 037207 (2008).

[69] F. J. Dyson, General theory of spin-wave interactions, Phys. Rev. **102**, 1217 (1956).

[70] S. S. Pershoguba, S. Banerjee, J. C. Lashley, J. Park, H. Ågren, G. Aeppli, and A. V. Balatsky, Dirac Magnons in Honeycomb Ferromagnets, Phys. Rev. X **8**, 011010 (2018).

[71] R. Albaridy, A. Manchon, and U. Schwingenschlögl, Tunable magnetic anisotropy in Cr–trihalide Janus monolayers, J. Phys.: Condens. Matter **32**, 355702 (2020).

[72] K. Zakeri, Terahertz magnonics: Feasibility of using terahertz magnons for information processing, Phys. C (Amsterdam) **549**, 164 (2018).

[73] H. J. Qin, S. Tsurkan, A. Ernst, and K. Zakeri, Experimental Realization of Atomic-Scale Magnonic Crystals, Phys. Rev. Lett. **123**, 257202 (2019).

[74] H. Liu, C. Zhang, H. Malissa, M. Groesbeck, M. Kavand, R. McLaughlin, S. Jamali, J. Hao, D. Sun, R. A. Davidson *et al.*, Organic-based magnon spintronics, Nat. Mater. **17**, 308 (2018).

[75] R. Shindou, J.-I. Ohe, R. Matsumoto, S. Murakami, and E. Saitoh, Chiral spin-wave edge modes in dipolar magnetic thin films, Phys. Rev. B **87**, 174402 (2013).

[76] R. Shindou and J.-I. Ohe, Magnetostatic wave analog of integer quantum Hall state in patterned magnetic films, Phys. Rev. B **89**, 054412 (2014).

[77] Y.-M. Li, J. Xiao, and K. Chang, Topological magnon modes in patterned ferrimagnetic insulator thin films, Nano Lett. **18**, 3032 (2018).

[78] B. Xu, T. Ohtsuki, and R. Shindou, Integer quantum magnon Hall plateau-plateau transition in a spin-ice model, Phys. Rev. B **94**, 220403(R) (2016).

[79] E. Iacocca and O. Heinonen, Topologically Nontrivial Magnon Bands in Artificial Square Spin Ices with Dzyaloshinskii-Moriya Interaction, Phys. Rev. Appl. **8**, 034015 (2017).

[80] P. Talatchian, M. Romera, F. A. Araujo, P. Bortolotti, V. Cros, D. Vodenicarevic, N. Locatelli, D. Querlioz, and J. Grollier, Designing Large Arrays of Interacting Spin-Torque Nano-Oscillators for Microwave Information Processing, Phys. Rev. Appl. **13**, 024073 (2020).

[81] J. F. Pulecio, P. Warnicke, S. D. Pollard, D. A. Arena, and Y. Zhu, Coherence and modality of driven interlayer-coupled magnetic vortices, Nat. Commun. **5**, 3760 (2014).

[82] C. C. Rusconi, M. J. A. Schuetz, J. Gieseler, M. D. Lukin, and O. Romero-Isart, Hybrid architecture for engineering magnonic quantum networks, Phys. Rev. A **100**, 022343 (2019).

[83] W. Cai, J. Han, F. Mei, Y. Xu, Y. Ma, X. Li, H. Wang, Y. P. Song, Z.-Y. Xue, Z.-Q. Yin, S. Jia, and L. Sun, Observation of Topological Magnon Insulator States in a Superconducting Circuit, Phys. Rev. Lett. **123**, 080501 (2019).

[84] K. Vogt, H. Schultheiss, S. Jain, J. E. Pearson, A. Hoffmann, S. D. Bader, and B. Hillebrands, Spin waves turning a corner, Appl. Phys. Lett. **101**, 042410 (2012).

[85] *Three-Dimensional Magnonics*, edited by G. Gubbiotti (Jenny Stanford Publishing, Singapore, 2019).

[86] T. Holstein and H. Primakoff, Field dependence of the intrinsic domain magnetization of a ferromagnet, Phys. Rev. **58**, 1098 (1940).

[87] D. Sticlet, F. Piéchon, J.-N. Fuchs, P. Kalugin, and P. Simon, Geometrical engineering of a two-band Chern insulator in two dimensions with arbitrary topological index, Phys. Rev. B **85**, 165456 (2012).

[88] M. Fruchart and D. Carpentier, An introduction to topological insulators, C. R. Phys. **14**, 779 (2013).

[89] J. C. Y. Teo, L. Fu, and C. L. Kane, Surface states and topological invariants in three-dimensional topological insulators: Application to Bi$_{1-x}$Sb$_x$, Phys. Rev. B **78**, 045426 (2008).

[90] W. A. Benalcazar, B. A. Bernevig, and T. L. Hughes, Electric multipole moments, topological multipole moment pumping, and chiral hinge states in crystalline insulators, Phys. Rev. B **96**, 245115 (2017).

[91] J. Langbehn, Y. Peng, L. Trifunovic, F. von Oppen, and P. W. Brouwer, Reflection-Symmetric Second-Order Topological

Insulators and Superconductors, Phys. Rev. Lett. **119**, 246401 (2017).

[92] Z. Song, Z. Fang, and C. Fang, $(d-2)$-Dimensional Edge States of Rotation Symmetry Protected Topological States, Phys. Rev. Lett. **119**, 246402 (2017).

[93] M. Geier, L. Trifunovic, M. Hoskam, and P. W. Brouwer, Second-order topological insulators and superconductors with an order-two crystalline symmetry, Phys. Rev. B **97**, 205135 (2018).

[94] S. H. Kooi, G. van Miert, and C. Ortix, Inversion-symmetry protected chiral hinge states in stacks of doped quantum Hall layers, Phys. Rev. B **98**, 245102 (2018).

[95] E. Khalaf, H. C. Po, A. Vishwanath, and H. Watanabe, Symmetry Indicators and Anomalous Surface States of Topological Crystalline Insulators, Phys. Rev. X **8**, 031070 (2018).

[96] C. Fang and L. Fu, New classes of topological crystalline insulators having surface rotation anomaly, Sci. Adv. **5**, eaat2374 (2019).

[97] L. Trifunovic and P. W. Brouwer, Higher-Order Bulk-Boundary Correspondence for Topological Crystalline Phases, Phys. Rev. X **9**, 011012 (2019).

[98] L. Fu and C. L. Kane, Topological insulators with inversion symmetry, Phys. Rev. B **76**, 045302 (2007).

[99] R.-J. Slager, A. Mesaros, V. Juričić, and J. Zaanen, The space group classification of topological band-insulators, Nat. Phys. **9**, 98 (2012).

[100] J. Kruthoff, J. de Boer, J. van Wezel, C. L. Kane, and R.-J. Slager, Topological Classification of Crystalline Insula-

tors through Band Structure Combinatorics, Phys. Rev. X **7**, 041069 (2017).

[101] H. C. Po, A. Vishwanath, and H. Watanabe, Symmetry-based indicators of band topology in the 230 space groups, Nat. Commun. **8**, 50 (2017).

[102] B. Bradlyn, L. Elcoro, J. Cano, M. G. Vergniory, Z. Wang, C. Felser, M. I. Aroyo, and B. A. Bernevig, Topological quantum chemistry, Nature (London) **547**, 298 (2017).

[103] S. Ono and H. Watanabe, Unified understanding of symmetry indicators for all internal symmetry classes, Phys. Rev. B **98**, 115150 (2018).

[104] T. L. Hughes, E. Prodan, and B. A. Bernevig, Inversion-symmetric topological insulators, Phys. Rev. B **83**, 245132 (2011).

[105] A. M. Turner, Y. Zhang, R. S. K. Mong, and A. Vishwanath, Quantized response and topology of magnetic insulators with inversion symmetry, Phys. Rev. B **85**, 165120 (2012).

[106] F.-Y. Li, Y.-D. Li, Y. B. Kim, L. Balents, Y. Yu, and G. Chen, Weyl magnons in breathing pyrochlore antiferromagnets, Nat. Commun. **7**, 12691 (2016).

[107] A. Mook, J. Henk, and I. Mertig, Tunable Magnon Weyl Points in Ferromagnetic Pyrochlores, Phys. Rev. Lett. **117**, 157204 (2016).

[108] Y. Su and X. R. Wang, Chiral anomaly of Weyl magnons in stacked honeycomb ferromagnets, Phys. Rev. B **96**, 104437 (2017).

[109] V. A. Zyuzin and A. A. Kovalev, Spin Hall and Nernst effects of Weyl magnons, Phys. Rev. B **97**, 174407 (2018).